ChemistrySelect

Review
doi.org/10.1002/slct.202504007

Chemistry Europe
European Chemical Societies Publishing

www.chemistryselect.org

Metal Ferrite/Biochar Nanocomposites for Dye Pollutant Removal: Insights into Adsorption and Photocatalytic Strategies

Hozefa Dhila,[a] Abhishek Bhapkar,[a] and Shekhar Bhame*[a]

The emergence of dye pollutants from industrial wastewater become a major environmental concern and posing significant threat to aquatic life and human health. Wastewater from several industries such as textiles, food production, fabric and leather tanning, cosmetics, paints manufacturing, paper and printing industries extensively use synthetic dyes that are highly resistant to degradation. Adsorption and photocatalytic degradation methods have emerged as promising approaches for the removal of dye pollutants from industrial wastewater. Various bio-based materials have been employed for the adsorption of dyes, among which biochar derived from various agricultural and forestry wastes observed as a sustainable and cost-effective material with high adsorption capacity. However, its limitation of slower adsorption rate, challenges of surface activation, regeneration capacity and post-treated slurry restricted their utilization in effective removal of dye pollutants. The loading of MFe_2O_4 nanoparticles on biochar produces synergistic effect of combined adsorption and photocatalysis for effective degradation of dyes. This review article delves into advancements in synthesis of MFe_2O_4/Biochar nanocomposites by various methods and highlight their characteristics. It further discusses the underlying mechanisms of adsorption and photocatalytic degradation of dye pollutants in the influence of various operational parameters such as adsorbent or photocatalyst dosage, initial dye concentration, pH and temperature.

1. Introduction

The increasing industrialization and urbanization have led to significant contamination of water bodies with various pollutants.[1,2] Among several organic pollutants, synthetic dyes are the most harmful contaminants due to their extensive use and complex structure.[3] Many research reports have highlighted the existence of wide range of dye pollutants including cationic and anionic dyes from various industries such as textile, food production, fabric and leather tanning, paints, paper and printing industries,[4] represented in Figure 1. Textile industries in particular generates significant level of dye effluents accounting for ~20% of global wastewater according to World Bank.[5] Several processes in textile production involved dyeing, printing, bleaching, and finishing consumes substantial amount of water and generates various harmful effluents and residues.[6] Since, every year thousand metric tons of dyes from these industries have been directly disposed into water bodies leading to water contamination due to longer persistence and resistant to biodegradation. Several synthetic dyes including cationic dyes such as malachite green, rhodamine B (RhB), crystal violet (CV), methylene blue (MB) and anionic dyes such as congo red (CR), methyl orange (MO), acid red, and direct blue (DB) are commonly found in industrial wastewater.[7]

Conventional methods of wastewater treatment such as filtration, ozonation, biosorption, membrane separation often fall short in effectively removing these contaminants.[8,9] Physical methods involved separation without chemical conversion and therefore, face limitations in addressing dye-specific challenges. Filtration, including ultrafiltration and membrane-separation such as reverse osmosis, often raise concerns associated with membrane fouling and reduces efficiency over time. High operational pressures, energy consumption, frequent cleaning or replacements make these methods expensive for large-scale applications. These methods are also very less effective in removal of soluble or low-molecular-weight dyes as well as complex dye molecules. In addition to these issues, membrane separation also generates concentrated reject streams that pose disposal problems and further contributing to secondary pollution.[10] Chemical methods such as oxidation and coagulation involved reactions to break down complex dye molecules. However, these methods often lacks efficiency in certain conditions and also lead to environmental contamination. Oxidation process employed hydrogen peroxide, persulphate (PS) or ozone, consumes high energy and increases overall operational cost. Oxidation process frequently produces secondary pollutants and toxic byproducts such as chlorinated

---

[a] *H. Dhila, A. Bhapkar, S. Bhame*
Materials Research Laboratory, Symbiosis Institute of Technology, Symbiosis International (Deemed University), Pune 412115, India
E-mail: shekhar.bhame@sitpune.edu.in

Abbreviations: AY17, Acid yellow 17; AO7, Acid orange 7; AB41, Acid blue 41; AB158, Acid blue 158; AC, Activated carbon; BC, Biochar; BBR, Bismarck brown; CR, Congo red; CV, Crystal violet; DR31, Direct red 31; DR80, Direct red 80; DB78, Direct blue 78; EBT, Eriochromie black T; GY-160, Golden yellow-160; IC, Indigo carmine; MB, Methylene blue; MFBC, Metal ferrite/Biochar; MG, Malachite green; Min, Minutes; MO, Methyl orange; MV, Methyl violet; NB, Nile blue; PR, Ponceau red; PS, Persulphate; RB4, Reactive blue 4; RB19, Reactive blue 19; RB5, Reactive black 5; RBR, Reactive brilliant red X-3B; RhB, RB, Rhodamine B; ROS, Reactive oxygen species; TZ, Tartrazine.

compounds, thereby imposing additional challenges for subsequent treatment.[11] Coagulation method typically involved alum or ferric salts, that generate large volumes of sludge and exhibit low removal of disperse or vat dyes while leaving residual toxicity in treated effluents.[12] Biological methods such as bioaccumulation and biosorption employ microorganisms or biomass to degrade dyes, however these approaches are unreliable and slow. These methods are limited by the resistance to microbial degradation of azo dyes owing to their recalcitrant and toxic to microbes. These methods also produce inconsistent results due to variable enzyme production and ineffective in high dye concentrations.[13,14]

Adsorption process involves binding dye molecules to adsorbent and outperforms conventional methods by providing high removal efficiency without generation of sludge and need of high-energy inputs.[15] These low-cost adsorbents derived from agricultural waste such as corn stalk, sugarcane bagasse, make it economically viable and applicable for removal of wide range of dye molecules, including cationic and anionic dyes. Unlike biological methods, adsorption is rapid and unaffected by toxicity of complex dye molecules, while also prevents generation of secondary pollutants. Several materials such as activated carbon (AC), graphene oxide, g-C_3N_4 and metal-organic frameworks (MOFs) enable selective and high-capacity removal further enhancing its sustainability. This method is a significant improvement over physical filtration, as it handles concentrated effluents better and requires less maintenance.[16,17] Photocatalysis stands out as an advanced oxidation process (AOP) in wastewater treatment.[18] It involves the activation of photocatalyst such as transition metal oxides under the UV or visible light illumination and generates reactive oxygen species (ROS) such as hydroxyl and superoxide radicals that break down complex dye molecules into simpler components like CO_2 and water.[19–21] It is environmentally friendly, leveraging solar energy for low operational costs making it more sustainable than energy-intensive conventional methods. High degradation rates are achieved, even for recalcitrant dyes, outperforming biological processes in speed and completeness.[22] Photocatalysis is characterized by high chemical stability, allowing the catalysts to function effectively over prolonged duration without significant degradation as well as negligible secondary pollution.[23] Metal oxide nanoparticles (such as ZnO, TiO_2, CuO) has been widely employed as a photocatalyst due to their physicochemical characteristics such as surface charge, high surface area-to-volume ratio, porous structure, tunable band gap, surface reactivity, and thermochemical stability for the adsorption and degradation of dye effluents.[24,25] However, the challenges of toxicity, reusability, and generation of secondary pollutants associated with metal oxides have drawn significant attention to researchers. This brings an urgency to explore the multivalent nanoparticles, in particular, iron-based nanoparticles, owing to its magnetic properties and high photocatalytic activity.[26]

Metal ferrites with the general formula MFe_2O_4 consist of divalent metal ions (M^{2+}, typically 3d transition metals) and

Hozefa Dhila is a Junior Research Fellow in the Department of Applied Sciences at Symbiosis Institute of Technology, Symbiosis International (Deemed University) under the supervision of Dr. Shekhar Bhame. He earned his B.Sc. in Chemistry from Pacific Academy of Higher Education and Research University Udaipur Rajasthan. He holds Master's degree in Chemistry from MIT World Peace University Pune, India. His research focuses on the Adsorption and Photocatalytic degradation of textile dyes using sustainable biochar-based nanocomposites.

Abhishek R. Bhapkar is a Senior Research Fellow and PhD researcher at Symbiosis Institute of Technology, Symbiosis International (Deemed University) Pune, India in the Department of applied sciences under the supervision of Dr. Shekhar Bhame. He earned his B.Sc. and M.Sc. in physics with specialization in materials science from Savitribai Phule Pune University. His research focuses on the photocatalytic degradation of textile dyes using cost-effective and easily synthesized metal oxides and their composites. He has published numerous research studies on ZnO–based photocatalysts for removal of textile dye pollutants from industrial wastewater.

Dr. Shekhar Bhame is an Assistant Professor in the Department of Applied Sciences at Symbiosis Institute of Technology (SIT), Symbiosis International (Deemed University) Pune, India. He completed his PhD from prestigious National Chemical Laboratory (NCL) Pune, followed by postdoctoral research at Nanyang Technological University (Singapore), CRISMAT Laboratory, CNRS (France), and the University of Liège (Belgium). With over 40 publications in reputed international journals, he also serves as a reviewer for several leading journals. His current research is centered on magnetic materials for sensing applications and photocatalytic treatment of textile wastewater.

Chemistry Europe
European Chemical Societies Publishing

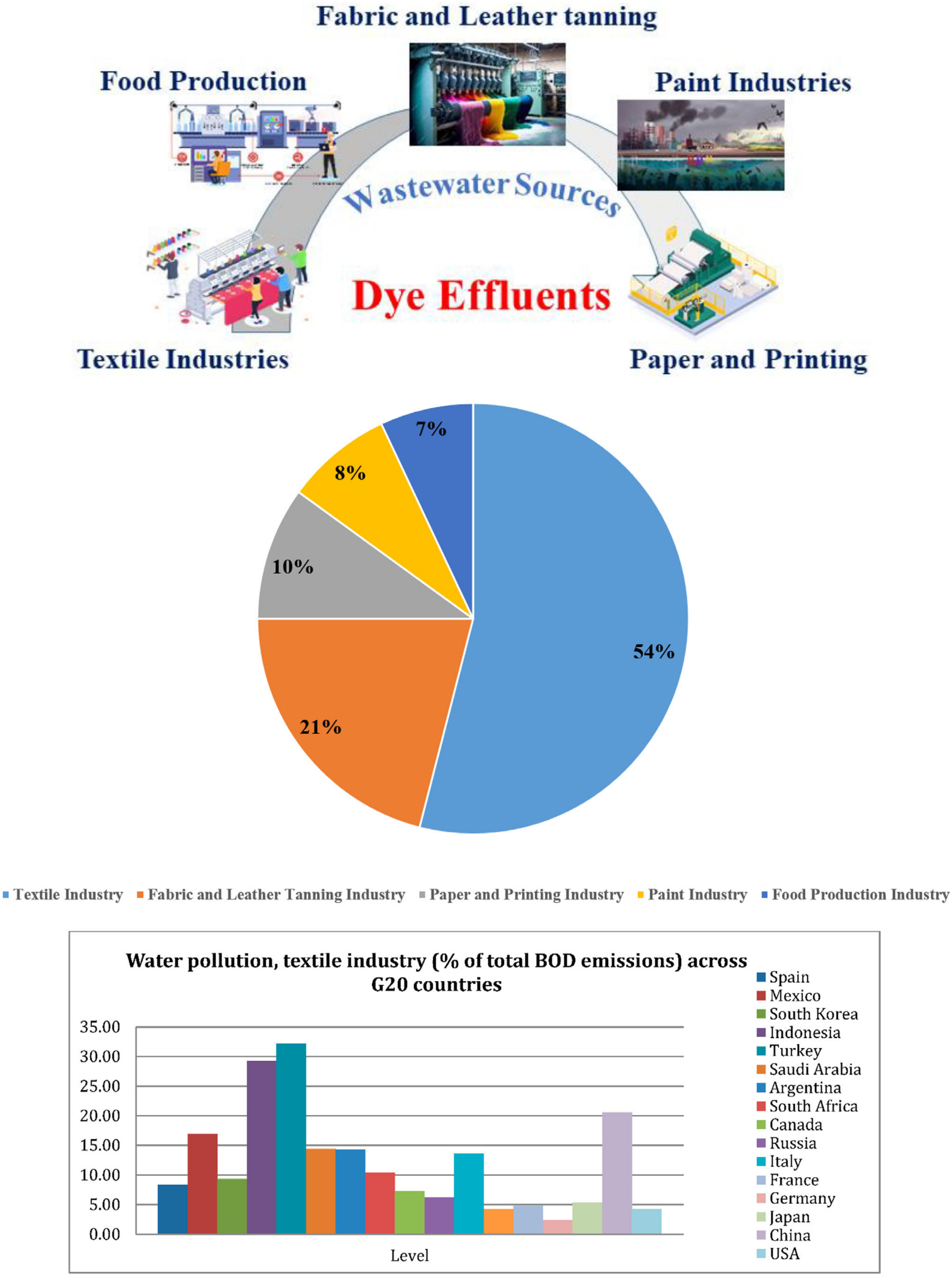

Figure 1. Dye effluents contribution from wastewater of various industries and %BOD emissions from textile industrial wastewater across G20 countries.[41] Reproduced under the terms of the CC BY 4.0 license. Copyright 2015, MDPI.

trivalent iron ions (Fe^{3+}) arranged in a spinel structure, where the selection of M^{2+} significantly influences the material's magnetic properties.[27] Spinel ferrites, MFe_2O_4 (M=Zn, Co, Ni, Cu, Mg or Mn) also exhibit remarkable stability over a wide pH range, more specifically in acidic pH which further support its utilization due to their resistance to corrosion and leaching for removal of pollutants from industrial wastewater.[28] In recent years, metal ferrites have been extensively explored by researchers as a heterogeneous photo-fenton catalyst for the photocatalytic degradation of organic pollutants from wastewater due to their intrinsic magnetic property, higher specific surface area, chemical stability, and easy recovery.[29] The catalytic activity of metal ferrites often attributed to the crystal field stabilization energies (CFSEs), although the specific surface area and band gap of a photocatalyst influences the catalytic activity. However the catalytic performance was also influenced by the CFSE which reflects the redox nature, structural stability, and photo induced charge separation efficiency.[30] Due to fine particle size, MFe_2O_4 easily aggregates and thus reduces the specific surface area and pore volume. The limited photocatalytic degradation efficiency of pure metal ferrites may also be attributed to the rapid recombination of photogenerated electron–hole pairs and slower kinetics of the redox coupling of Fe^{2+}/Fe^{3+}. This could be due to relatively lower band gap of MFe_2O_4, compared to commonly employed metal oxide photocatalyst such as ZnO and TiO2 with band gap of 3.37 eV and 3.2 eV, respectively,[31] while the band gap of $ZnFe_2O_4$, $CuFe_2O_4$, $CoFe_2O_4$, $NiFe_2O_4$ are 1.91 eV, 1.89 eV, 2.31 eV, 2.2 eV respectively.[32] These challenges have been overcome either by suitable doping strategies or by using biochar as a carrier to support MFe_2O_4 nanoparticles. The doping of elements into crystal lattice of spinel ferrites significantly enhances its electronic, structural, and surface properties that influence the photocatalytic kinetics and stability of catalyst. Doping strategies accelerate reaction kinetics by tuning the bandgap, enhancing charge carrier mobility, and increasing the number of active sites, which promote faster pollutant degradation under light irradiation.[33] For instance, the doping of sulphur in $CuFe_2O_4$ decreases the bandgap from 1.80 eV to 1.78 eV, which led to increase the degradation efficiency of RhB dye from 65% to 99% and 64% to 98% for CR within 100 min whereas for MO from 63% to 97% in 70 min.[34] Similarly, in another study, 3% sulphur doping in $MnFe_2O_4$ decreases the bandgap gap from 2.20 eV to 2.11 eV that significantly shows 100% degradation of methylene blue within 135 min on exposure to sunlight. Furthermore, doping introduces intermediate energy levels within the band structure, narrowing the bandgap, and extending light absorption from the UV to the visible region. This promotes efficient electron-hole pair generation and accelerate redox reactions. The photocatalytic stability of ferrite-based composites was highly influenced by doping in terms of structural integrity, thermal resistance, and reusability, however excessive doping may also result in phase impurity as well. The sulphur doping in $MnFe_2O_4$ helps in retaining 94% degradation efficiency even after 6 cycles and possess low charge-transfer resistance with enhanced interfacial stability.[35] Similarly, S doping in $CuFe_2O_4$ showed excellent thermal stability and recyclability over 3 cycles for degradation of MO dye.[34]

Biochar was utilized as a carrier owing to its higher specific surface area and porous structure and prevent the agglomeration of MFe_2O_4 nanoparticles. The biochar support enhances the charge separation efficiency and thereby suppressing the rapid recombination of e^-/h^+ pairs. The biochar support also provide a medium for the migration of photogenerated electrons and accelerate the redox cycling of MFe_2O_4, thereby improving the overall photocatalytic degradation efficiency of spinel ferrites.[36] The carbon-based materials such as biochar are widely utilize and shows high efficiency in adsorption of pollutants due to their large surface area.[37] The challenges in improving the adsorption capacity of biochar has been an interesting subject in recent times.[38] Several techniques have been employed by researcher in modifying the biochar with the suitable material to improve its adsorption capacity for remediation of pollutants.[39] In these context, biochar has been explored as a supporting material for metal ferrites (MFe_2O_4) as it inhibit the agglomeration of ferrites and enhances the adsorption capacity.[29] MFe_2O_4 modified biochar nanocomposites have been emerged as promising materials due to their unique properties, including high surface area, magnetic separation capabilities, surface functional groups, and enhanced adsorption and photocatalytic activities. These nanocomposites remediate various dye pollutants from industrial wastewater, due to their interesting physiochemical properties. Metal Ferrite/Biochar (MFBC) nanocomposites have exhibited excellent adsorption capacity and photocatalytic activity and intrinsic magnetic property that ease an extraction and separation of slurry under applied magnetic field in water purification process. In recent study, biochar derived from lemon peels supported Mn-doped $CaFe_2O_4$ nanoparticle by hydrothermal method. The Mn-doping significantly enhanced the photocatalytic activity by introducing intermediate energy levels within the band gap, preventing the rapid recombination of e^-/h^+ pairs while biochar act as carrier to facilitate the electronic charge transfer. This nanocomposite employed for the photocatalytic degradation of Rhodamine B dye under the simulation of sunlight and shows remarkable photogradation efficiency of 97.31% within 70 min using 0.1 g/L of photocatalyst dose.[40] This article review the recent advancement and progress in the application of MFBC nanocomposites in adsorption and photodegradation of dye pollutants. It also discusses various synthesis methods, characteristics, advancement in adsorption capacity and photocatalytic activity, and enhancement in dye removal efficiency. The underlying mechanisms associated with MFBC employed as heterogenous Fenton-like H_2O_2 and PMS/PDS-activated photocatalyst for the degradation of various dye pollutants from industrial wastewater have been comprehensively discussed. This review also addresses current challenges and offers insights to potential future prospects for further advancements in development of MFBC nanocomposites.

Figure 2. Various biomass feedstock for biochar production.[24] Reproduced under the terms of the CC BY-NC-ND license. Copyright 2025, Elsevier.

2. Biochar: Sources and Characteristics

Biochar are carbonaceous materials produced by pyrolysis of biomass materials in anaerobic environment at high temperature. The production of biochar from agricultural and municipal wastes as well as from industrial and forestry residues through pyrolysis, torrefaction, hydrothermal carbonization, and gasification, practiced for large-scale production of biochar.[42] The production of biochar often recognized as a sustainable solution in managing organic waste, improving soil fertility, generation of bioenergy, and in rehabilitate degraded sites.[43] These preparation methods not only influence the physicochemical and functional properties but also influences the applications of biochar. The essence of biochar-based nanocomposites has been governed by type of biomass feedstock and pyrolysis conditions that influences its properties including specific surface area, porous structure and functional groups. The decomposition and pyrolysis of biomass over a specific temperature range typically between 300 °C and 1200 °C significantly influence the adsorption efficiency. However, the pyrolysis temperature used to be maintained in a range from 300 °C to 700 °C as it helps in retention of the nutrients, volatile matter, optimum carbon content as well as the surface functional groups that enhances the adsorption process. Increasing the pyrolysis temperature results in increased surface area and porosity but it may lead to the loss of essential surface functional groups and decreasing of adsorption capacity.[44–46] Biochar derived from pyrolysis of agricultural and industrial waste, forestry residues, sludge and municipal waste (Figure 2) with adequate surface area, uniform pore size, and volume and multifunctional groups has ideally remove wide range of pollutants from industrial wastewater. The structural and functional properties of biochar can be improved by chemical treatment by acids, alkalis, metal salts, and oxides enhancing the adsorption capacity by the increasing specific surface area and porosity.[47] The presence of oxy/hydroxyl-functional groups on the surface of biochar such as carboxyl (–COOH), hydroxyl (–OH), carbonyl (C=O), and phenol groups enhances reactivity as well as adsorption capacity.[48]

3. Synthesis and Characterizations of Metal Ferrite/Biochar nanocomposites

The production of biochar from renewable biomass feedstock reduces the carbon footprint while the nontoxicity, abundancy, and synthesis of metal ferrites via environmentally benign methods offer a sustainable approach for remediation of pollutants.[49,50] Interestingly, the adsorption capacity of MFBC nanocomposite has been much higher than pure biochar owing to their chemical stability, porosity, and higher active sites. The synthesis approach and the amount of precursor of metal ferrite and biochar has significantly influence the adsorption performance as well as the photocatalytic activity of MFBC nanocomposites.

3.1. Synthesis of MFe_2O_4/BC Nanocomposites

Metal ferrites (MFe_2O_4) have been emerged as significant nanoparticles in removal of contaminants such as organic pollutants from textile industrial wastewater. Spinel ferrites have gained considerable attention as a photocatalyst due to remarkable lower energy band gaps, which make its effective utilization on exposure to visible light.[27,32] On the other hand, Biochar has been explored as an excellent adsorbent owing to high porous structure, specific surface area and oxygen containing surface functional groups which enhances the interaction of dye pollutants.[51,52] The impregnation of metal ferrites into biochar matrix prevents aggregation while the uniform dispersion of MFe_2O_4 nanoparticles also ensures its superior stability that accounts for its regeneration and reusability. Further, MFe_2O_4 also enhances the adsorption capacity by facilitating additional active sites for the adsorption of dye molecules. The integration of MFe_2O_4 into biochar matrix has not only decreases the band gap but also reduces the rapid recombination of photogenerated electron-hole pairs that affects the photocatalytic activity. The synthesis of MFBC nanocomposites involve diverse techniques and methodologies, primarily include chemical approaches, such as co-precipitation, hydrothermal, sol-gel, and auto-combustion. Each providing specific advantages in tailoring properties such as particle size, morphology, degree of crystallinity, phase purity, and surface properties.[53] The stability and practical feasibility of MFBC nanocomposite largely depends upon their resistance to agglomeration, specific surface area, and desorption efficiency over multiple regeneration cycles. For instance, $MnFe_2O_4$/OPBC synthesized by co-precipitation method exhibited mesoporous structures with Brunauer–Emmett–Teller (BET) surface areas ranging from 97.2 to 181.2 m^2/g and pore volumes of 0.09–0.30 cm^3/g. The pH adjustment to 10 in co-precipitation step improved crystallinity and prevented aggregation, leading to higher porosity with average pore sizes of 6.21–9.33 nm compared to pristine biochar while also enhanced adsorption capacity to 46.90 mg/g.[54] The overview, advantages, limitations and synthesis-property performance trade-offs of various methods employed for the synthesis of MFBC nanocomposites such as co-precipitation, hydrothermal, sol-gel, and auto combustion summarized in Table 1.

3.1.1. Co-precipitation

The co-precipitation technique has been often employed for the synthesis of MFBC nanocomposites due to its cost-effectiveness and high yield. This method involves mixing metal salts (precursors) with biochar in the presence of a solvent to achieve uniform dispersion and stabilization. However, challenges such as controlling particle size, preventing aggregation, and ensuring purity remain significant limitations of this approach. The nanocomposite of manganese ferrite and zinc ferrite was capped with *Chromolaena odorata* biochar using the co-precipitation method, demonstrated excellent environmental and biological compatibility by reflecting photoadsorption of indigo carmine (IC) and methylene blue dyes in presence of solar irradiations and also non-inhibition of bacterial growth. The co-precipitation method yield small crystallite size that allows uniform distribution of $MnFe_2O_4$ over BC surface, leads to higher number of active sites, while the higher BET surface area of 197.64 m^2/g in $MnFe_2O_4$/BC than $ZnFe_2O_4$/BC (92.14 m^2/g) shows better adsorption capacity of 173.5 mg/g for IC and 131.6 mg/g for MB.[55] The magnetic biochar derived from snake fruit peel synthesized by co-precipitation method followed by carbonization under N_2, exhibited a band gap of 2.23 eV and surface area of 126 m^2/g that supports its utilization for photocatalytic degradation of RhB dye. Furthermore, the Vibrating sample magnetometry (VSM) analysis represent its superior magnetic characteristics with saturation magnetization (Ms) of 24.2 emu g^{-1} enabling its reusability over five cycles while also maintaining 99.9% RhB degradation efficiency in 15 min under UV light.[56]

3.1.2. Sol-Gel

Sol-gel method is also an attractive and widely employed technique for the synthesis of MFBC nanocomposite due to its versatility, homogeneity, controlled particle size and uniform dispersion of nanoparticles.[57] Sol-gel method allows precise control over surface morphology, crystallinity, and particle size of nanocomposite. This method typically involves the transition of a system from a sol—a colloidal suspension of precursor particles—to a gel, characterized by a 3D network of crosslinked metal–oxygen bonds. For instance, the synthesis of $CuFe_2O_4$/biochar nanocomposite via sol-gel technique shows improved morphology as $CuFe_2O_4$ scattered uniformly over the biochar pores and also prevent agglomeration, enhancing the photocatalytic activity for degradation of MB, MO, and Tartrazine (TZ) dyes under visible light irradiations.[58] In another study, Leichtweis et al., adopted similar approach to dope $CuFe_2O_4$ nanoparticles in malt bagasse biochar for degradation of RhB dye by photo-fenton process.[59] In $ZnFe_2O_4$-based nanocomposite, $ZnFe_2O_4$ NPs were supported by chitin-residue biochar and fabricated by sol-gel method to degrade RhB dye using photo-fenton process. It was observed that chitin biochar does not only prevents the $ZnFe_2O_4$ nanoparticle aggregation but also facilitate the interaction of these nanoparticles to surface functional groups present on its surface.[60] Zn-doped $CuFe_2O_4$@biochar composite synthesized by sol-gel pyrolysis technique was implemented as PS activator for photocatalytic degradation of CV dye. Zn doping and *Eucalyptus* plant-based biochar support in $CuFe_2O_4$ enhances the specific surface area and thus increases the number of active sites. Further, Zn doping also leads to lattice distortion and generate more oxygen vacancies whereas it also increases magnetic properties of nanocomposites as

Table 1. Overview, advantages, and limitations of various methods employed for synthesis of MFBC nanocomposites.

Methods	Overview	Advantages	Limitations	Synthesis-property-performance trade-Offs
Hydrothermal	Crystallization of substances at higher temperature and pressure in autoclave	Control over the size, shape, and high crystallinity of nanoparticles	High energy demand, need autoclave reactor, not applicable to large scale production	Formation of highly crystalline, well-dispersed ferrites that significantly enhances photocatalytic activity, however energy cost and scalability limit industrial feasibility
One-step Pyrolysis	Impregnation of biomass with metal ferrite precursors and subjected to pyrolysis. In-situ formation of MFBC	Energy efficient, cost-effective, eco-friendly, large-scale applicability	High temperature may cause agglomerations and loss of surface functional groups, No control over particle size	Anchoring of metal ferrites over biochar matrix improves stability and recyclability, but loss of functional groups and specific surface area reduces active sites and thus decreases overall adsorption/photocatalytic performance
Sol-gel	Transitioning from a liquid “sol” into a solid “gel” phase	Precise control over the composition and morphology and, and uniform distribution of particles	High-temperature calcination may degrade surface functional groups, formation of byproducts	Enables molecular-level controlled morphology and yields uniform MFBC with tunable surface properties, however biochar degradation during calcination reduces adsorption efficiency
Co-precipitation	Metal salts co-precipitated with base (NaOH/NH_4OH) in presence of biochar	Simple, scalable, low cost, produces higher surface area in MFBC	Limited control over particle size and morphology, excessive product loss during washing	Economical and rapid synthesis route, delivers favorable initial properties, however low crystallinity and agglomeration limit long-term performance; while annealing improves stability at the expense of surface functional groups.

observed by the increase of saturation magnetization (Ms) in nanocomposite. The increasing number of oxygen vacancies enhances the rapid migration of electrons to generate ROS radicals that could enhance the overall photocatalytic activity of nanocomposite.[61] Ultrasonic assisted sol-gel technique was employed in loading lanthanum ferrite ($LaFeO_3$) nanoparticles on peanut shell derived biochar, modified the lamellar structure of BC to a porous structure. Further, the loading of $LaFeO_3$ also increases the specific surface area, micropores, and pore volume as determined by BJH method in BET analysis that enhances the adsorption capacity. $LaFeO_3$/BC nanocomposite was employed as bisulfite (BS) activator to degrade MB dye.[62] A magnetic adsorbent synthesized via sol–gel method by coating $CuFe_2O_4$ nanoparticles onto biochar derived from tea waste.

3.1.3. Hydrothermal Method

Hydrothermal synthesis involves the reactions in an aqueous solution containing MFe_2O_4 and biochar precursors at high temperatures and pressures within a sealed stainless-steel reactor (autoclave). By surpassing water's boiling point, this process leverages the unique properties of superheated or supercritical water, enhancing reaction kinetics and precursor solubility. Beta vulgaris (sugar beet) leaves extract was utilized to fabricate $CuZnFe_2O_4$@N,S-doped biochar composite via one-pot hydrothermal strategy. Initially, the plant extract was added to precursors of metal ferrites and further these leaves were also utilized to prepare N, S doped biochar. The N, S doping in pristine biochar contributed in increasing the pore size by forming aggregated irregular shapes on biochar surface that interact with CZF nanoparticles and helps in binding and removal of azo dyes.[63] Biochar derived from waste bamboo powder was activated using NaOH to obtain porous biochar and magnetized by loading $CoFe_2O_4$ nanoparticles using hydrothermal method. Further, it was modified by impregnating polyethyleneimine to enhance the adsorption capacity. The dispersion of $CoFe_2O_4$ nanoparticles over biochar pores enhances the specific surface area (S_{BET}) to 42.329 m^2/g from 15.113 m^2/g of pristine BC as well as pore volume from 0.016 cm^3/g of pure BC to 0.142 cm^3/g of $CoFe_2O_4$/BC nanocomposite, increasing the adsorption capacity to 899.44 mg/g.[64] $MnFe_2O_4$/BC nanocomposite synthesized via one-step hydrothermal strategy was employed as ultrasonic-assisted heterogenous catalyst to degrade MB and RhB dyes. The fine size and relatively strong magnetic property of $MnFe_2O_4$ lead to the agglomeration and further reducing the reactivity that affects the catalytic performance. To overcome the challenge of aggregation, biochar derived from poplar wood powder was utilized as a carrier that further increases the specific surface area of nanocomposite from 41.4 m^2/g (of pure $MnFe_2O_4$) to 95.1 m^2/g.[65,66] A ternary nanocomposite of biochar/$NiFe_2O_4$/Ag_3PO_4 was fabricated using hydrothermal method for removal of Hg and degradation of MB dye. Biochar derived from sugarcane waste was used as a supporting material for enhancing the stability of Ag_3PO_4 and $NiFe_2O_4$ while also enhanced the specific surface area S_{BET} to 79.48 m^2/g as compared to 11.27 m^2/g of pure biochar. The presence of surface multifunctional oxy groups and higher specific surface area combined to enhance the adsorption capacity as well as photocatalytic degradation efficiency.[67] Amino-functionalized rice bran biochar/$MgFeAlO_4$ (RB@$MgFeAlO_4$-NH_2) composite synthesized by one-step solvothermal approach beneficial in preventing nanoparticle aggregation, while preserving strong saturation magnetization value of 19.78 emu/g ensures easy separation.[68]

3.1.4. One-Step Pyrolysis

One-step pyrolysis is an eco-friendly, energy efficient, and simplified approach for the fabrication of MFBC nanocomposite. It involved the direct thermal decomposition of metal precursors and biomass in a single step under the inert N_2 atmosphere. For, e.g., *Peganum harmala* powder directly added to the solution of Mn^{2+}, Zn^{2+}, and Fe^{3+} nanoparticles precursors and NaOH to form a viscous gel solution and subjected to pyrolysis under N_2 atmosphere at 600 °C to prepare Mn-$ZnFe_2O_4$/biochar nanocomposite for the adsorption and photocatalytic degradation of RhB dye. The single-step impregnation and pyrolysis ensures uniform distribution of MFe_2O_4 into biochar matrix while also prevents aggregation of nanoparticles, however the preferable morphology and retention of surface functional groups required for adsorption of dye pollutants need to be addressed for higher adsorption and photocatalytic degradation efficiency.[69] In another study, Eucalyptus sawdust added between Zn^{+2} and Fe^{+3} precursor solution under constant stirring and further pyrolyzed in tubular furnace at 600 °C under N_2 atmosphere for 120 min. to form $ZnFe_2O_4$/Biochar nanocomposite for the adsorption and photo-fenton degradation of the RB and RBR dyes.[48] In situ formation of $CoFe_2O_4$ on biochar from agricultural wastes (sunflower husks (SH), Rice, and Peas) in one-stage process using nitrates, ammonia, and citric acid formed octahedral crystals with a reversal parameter (λ) of 0.1–0.9, influencing magnetic inversion and specific surface area (83–116 m^2/g). Higher λ (0.9) of $CoFe_2O_4$/SH and $CoFe_2O_4$/Rice (0.85) form inverse spinel whereas $CoFe_2O_4$/Peas ($\lambda = 0.1$) likely to form normal spinel and thus inverted spinels tends to create more active sites for the adsorption. Henceforth, $CoFe_2O_4$/SH shows higher adsorption capacity of 6.98 mg/g compared to $CoFe_2O_4$/Peas (1.22 mg/g).[70]

3.2. Characterizations of MFe_2O_4/Biochar Nanocomposites

The physicochemical properties, surface morphology, structural characteristics, and elemental compositions of MFBC nanocomposites have been studied by various characterization techniques such as Fourier transform infrared spectroscopy (FTIR), Field emission-scanning electron microscopy (FE-SEM) and Transmission electron microscopy (TEM), X–ray diffraction (XRD), X- ray photoelectron spectroscopy (XPS), Raman spectroscopy, VSM, and BET as shown in Figure 3 and 4. XRD analysis determine the crystallinity index and phase purity of MFBC nanocomposites. The broad diffraction peak indicates the amorphous and graphitic layered region of biochar, observed around 23° corresponds to (002) plane and 43° correspond to (100) plane, while the sharp and well-defined peaks represent high degree of crystallinity of $ZnFe_2O_4$ observed at 18.2°, 29.9°, 35.2°,

Review
doi.org/10.1002/slct.202504007

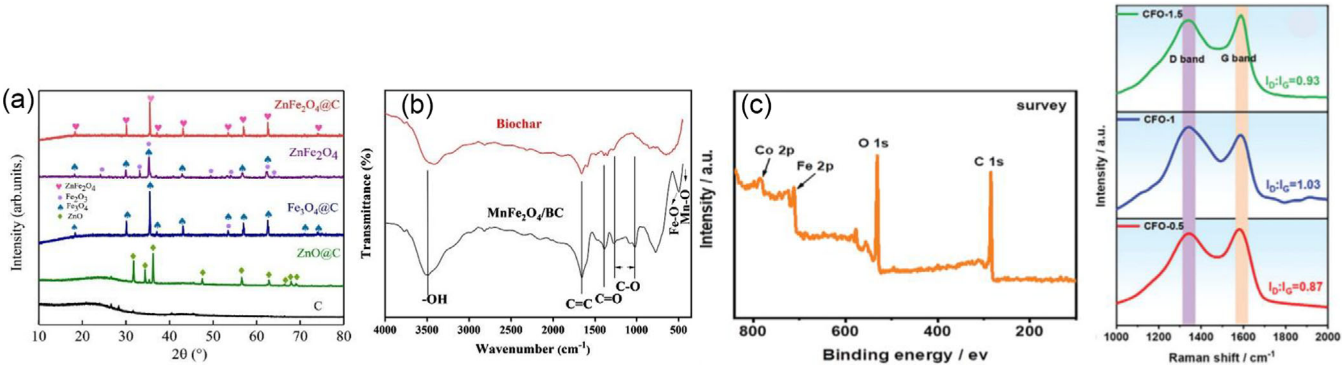

Figure 3. a) XRD patterns of $ZnFe_2O_4$@BC, Reproduced with permission from[71] Copyright 2024, Elsevier. b) FTIR spectra of BC and $MnFe_2O_4$/biochar. Reproduced with permission from[66] Copyright 2021, Elsevier. c) XPS spectra of $CoFe_2O_4$/BC and d) Raman spectra of $CoFe_2O_4$/BC, Reproduced with permission from[75] Copyright 2024, John Wiley and Sons.

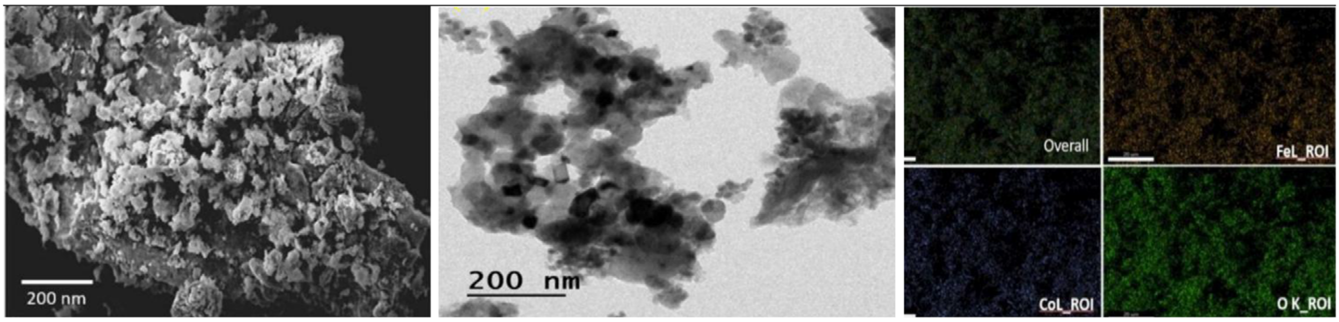

Figure 4. SEM, TEM, and element mapping of Fe, Co, and O of $CoFe_2O_4$/Biochar composite. Reproduced with permission from[78] Copyright 2025, Elsevier.

36.8°, 42.8°, 53.1°, 56.6°, 62.2° and 74.5° correspond to (111), (220), (311), (222), (400), (422), (511), (440), (622) planes. The diffraction peaks between 23° and 29.9° suggest the formation of hybrid $ZnFe_2O_4$/BC nanocomposite that retains the characteristics of amorphous region of carbonaceous biochar alongside with crystalline nature introduced by $ZnFe_2O_4$.[71]

The surface morphology and structural characteristics of MFBC is analyzed by FE-SEM. The SEM analysis of biochar derived from beta vulgaris leaves exhibit well-structured uniform outer layer with interconnected nanoscale pores whereas Cu doped $ZnFe_2O_4$ exhibit sheet-like layered structure that enhances the surface area, while N,S-doping increases the pore size, account for higher adsorption.[63] Conversely, it may also be challenging to analyze the loading of $ZnFe_2O_4$ over BC surface via SEM, in such a case HR-TEM analysis revealed the binding of $ZnFe_2O_4$ on biochar surface by demonstrating cubical structure of diameter 60–80 nm, characterized lattice d-spacing between 0.44 nm and 0.29 nm corresponding to lattice planes of (111) and (311) of $ZnFe_2O_4$.[72] The generation of honeycomb-like structure of pores and micropores in $ZnFe_2O_4$@AC nanocomposite analyzed by FE-SEM, can be advantageous in enhancing the adsorption of RhB, MO, and AY-17 dyes.[73] The SEM analysis of AC derived from *Phoenix dactylifera* date stones shows rough surface, which transformed to porous heterogeneous surface upon loading of spherical $CoFe_2O_4$ nanoparticles increasing the adsorption of cationic MB and MV dyes.[74]

X- ray photoelectron spectroscopy (XPS) analysis of MFBC involved the survey spectrum that reveals the surface elemental composition while the high-resolution spectra providing insights to the oxidation states of each element. The XPS spectra of MFe_2O_4/biochar confirms the presence of carbon (C), Oxygen (O), Nitrogen (N), Iron (Fe), and a divalent metal (M). The C 1s peak observed in biochar reflects the structural composition and chemical bonding of carbon that distinguished by aromatic (sp^2) and aliphatic (sp^3) carbon to understand the degree of graphitization in MFBC nanocomposites. For instance, the XPS spectra of $CoFe_2O_4$@BCNPs shows three distinct peaks in C 1s spectrum at 285.5 eV (C═O), 284.5 eV (C–O–C), 284.1 eV (C–C/C═C). The O 1s spectra exhibited three distinct photoelectron signals i.e., at 533.4 eV that correspond to adsorbed oxygen, 531.9 eV to the oxygen vacancy, and 530.4 eV to lattice oxygen. The presence of Co and Fe in $CoFe_2O_4$/BC nanocomposite was confirmed by peaks of Co between 803.1 eV and 786.8 eV along with two distinct peaks of Fe between 724.3 eV and 710.3 eV correspond to $2p_{1/2}$ and Co $2p_{3/2}$ respectively. The binding energy shift suggesting electron e transfer as well as interfacial interaction between $CoFe_2O_4$ and biochar.[75]

The structural analysis of surface functional groups and their chemical interactions in MFBC nanocomposite is observed in FTIR spectrum.[76] Biochar exhibit characteristic absorption peaks associated with various surface functional groups such as carbonyl (–C═O), hydroxyl (–OH), carboxylate (O–C═O) groups influenced by the biochar feedstock, pyrolysis temperature, and chemical or physical modifications. These functional groups play a crucial role in the physicochemical properties of biochar, influencing its adsorption capacity, chemical reactivity, and interactions with other materials. In $MnFe_2O_4$/BC composite, peaks between 459 cm^{-1} and 580 cm^{-1} were associated to Mn–O and Fe–O stretching vibrations, respectively indicating the formation of a spinel-type structure. The broad absorption bands in the 3450–3400 cm^{-1} region were assigned to –OH stretching vibrations, which were more intense in the $MnFe_2O_4$/BC spectrum than in pure BC, due to the presence of surface-bound hydroxyl groups and metal–OH interactions, which ultimately has a key role in radical formation during the Fenton-like reaction. The peaks between 1640 cm^{-1} and 1400–1450 cm^{-1} corresponding to C═C aromatic stretching and C═O stretching of carboxylic groups, respectively. These groups are inherent to biochar and contribute to the dispersion and stabilization of nanoparticles through surface complexation. The reduction in the C–O stretching peak (1300–1000 cm^{-1}) intensity in the composite compared to pure BC suggested the possible formation of M–O–C bonds, indicating chemical interactions between $MnFe_2O_4$ and the biochar surface.[66]

Raman spectroscopy provides valuable insights into the A_1g mode correspond to symmetric stretching vibrations of metal-oxygen bonds at tetrahedral sites in MFBC composites while it also shows characteristic Raman peaks associated with the defective or disordered carbon in biochar represented by the D-band (sp^3-hybridized carbon) and in-plane graphitized carbon vibration by G-band (sp^2-hybridized carbon). For, e.g., In $CoFe_2O_4$/biochar, the Raman spectra revealed peaks between 1340 cm^{-1} and 1590 cm^{-1}, associated with the D-band and G-band indicate the presence of defective and graphitic carbon originating from biochar. The I_D/I_G ratio, which serves as an indicator of carbon defect density was 1.03 for $CoFe_2O_4$/biochar, suggesting higher level of structural disorder.[75] Similarly, the Raman spectra of $CoFe_2O_4$/AC (AC derived from *P. dactylifera* date stones) exhibits the D-band at 1355 cm^{-1} and the G-band at around 1586 cm^{-1}. The I_D/I_G ratio of $CoFe_2O_4$/AC nanocomposite and AC determined between 0.847 and 0.854 respectively, implying that nanocomposite has lower sp^2 carbon content than AC due to the incorporation of $CoFe_2O_4$ over biochar.[74] $MnFe_2O_4$/biochar exhibit peak at 620 cm^{-1} corresponding to symmetric vibration of M–O bond and two prominent peaks were observed between 1336 cm^{-1} (D-band) and 1580 cm^{-1} (G-band) signifies the lattice defects and vibrational sp^2-hybridized carbon respectively.[77] Hence, Raman spectral analyses highlight the structural modifications induced by the incorporation of different MFe_2O_4 phases into biochar, influencing its disorder and defect characteristics. Furthermore, the observed variations in the I_D/I_G ratio provide critical information for evaluating the degree of graphitization and the potential catalytic mechanisms of MFBC nanocomposites.

4. Adsorption and Photocatalytic Properties of MFBC Nanocomposites

4.1. Zinc Ferrite/Biochar Nanocomposites

Metal ferrites are soft magnetic materials with diversified properties that shows promising application as photocatalyst and adsorbent material for dye remediation from wastewater. Among various spinel ferrites, zinc ferrite has been widely investigated as photocatalyst due to its chemical stability, nontoxicity, inherent magnetic properties, and narrow band gap of 1.9 eV. The lower band gap energy enables it to absorb visible light, however, the rapid recombination of photogenerated electron-hole pairs can reduce the photocatalytic efficiency. Therefore, researcher have developed various nanocomposites using $ZnFe_2O_4$ with biochar material that result in the formation of heterojunction structure for enhance photocatalytic response under visible light. Biochar also offers the extensive specific surface area that helps in preventing aggregation of loaded $ZnFe_2O_4$ nanoparticles on biochar surface. Table 2 represents degradation of various dye pollutants by $ZnFe_2O_4$/BC nanocomposites.

Abdelfatah et al. investigates the effectiveness of a novel magnetic, cleaner, and sustainable composite, $CuZnFe_2O_4$@N,S-doped biochar (CZF@N,S-BC), in the removal of reactive black dye 5 (RB5) as represented in Figure 5. CZF@N,S-BC exhibited higher adsorption capacity of more than 50% and 100 mg/g respectively for certain dyes, such as RV 03 and DGV 1. In contrast, the adsorption rates of other dyes, such as DBV 44, BR 19, and RR 120 were very low, less than 40% and 80 mg/g. Furthermore, the adsorption of RB5 onto the nanocomposite showed much higher efficiency and capacity compared to the other dyes with an adsorption efficiency of 88.25% and a capacity of 176.50 mg/g.[63] In another study, $ZnFe_2O_4$ and $MnFe_2O_4$ NPs were capped with biochar derived *Chromoleana odorata* weeds for the photosorption of IC and MB dye. The biochar capping significantly reduces the band gap from 3.63 eV to 2.08 eV for $MnFe_2O_4$/BC, while 2.53 eV for $ZnFe_2O_4$/BC, which enhances its response to visible light. The mesoporous architecture of $MnFe_2O_4$/BC and $ZnFe_2O_4$/BC also studied for the adsorption behavior of IC and MB dyes by different isotherm model. The adsorption of IC followed intraparticle diffusion kinetics and best fitted in nonlinear Langmuir model for $MnFe_2O_4$/BC with maximum adsorption capacity of 173.47 mg/g, while it follows pseudo-second-order kinetics in $ZnFe_2O_4$/BC with maximum adsorption capacity of 129.91 mg/g. In contrast, the adsorption of MB follows pseudo-first-order kinetics and describe well by linear Langmuir model with adsorption capacity between 131.58 mg/g and 123.46 mg/g for $MnFe_2O_4$/BC and $ZnFe_2O_4$/BC respectively. The narrow band gap ultimately promotes the excitation of electrons as less energy required for migration from VB to CB and lead to generate more reactive radicals for photodegradation of IC and MB. The photocatalytic study reveals 98.60% removal of MB (30 ppm) by $ZnFe_2O_4$@BC (1.0 g/L) and 77.65% removal of IC (30 ppm) by $MnFe_2O_4$@BC (1.0 g/L) within 120 min under visible light irradiation.[55] Mn substituted $ZnFe_2O_4$/magnetic biochar nanocomposite was prepared by Alharbi et al. using one-step pyrolysis method to remove RhB dye. The adsorption of RhB carried out by using 3.2 g/L dosage of nanocomposite under pH 4 and result in 82% removal of 10 ppm RhB within 90 min. The adsorption process follows pseudo-second-order kinetics and best described by the Langmuir isotherm with a maximum adsorption capacity of 34.5 mg/g. The photocatalytic degradation involved photo-Fenton method and additionally H_2O_2 for the removal of RhB. 2.5 g/L of nanocomposite was employed to

Table 2. Adsorption and Photocatalytic degradation of dyes by Zinc ferrite/Biochar nanocomposites.

Catalyst	Catalyst dosage (g/L)	Synthesis method	Biochar source	Dye	Initial dye conc. (ppm)	Light source	Reaction time	pH	Adsorption capacity (mg/g)	% dye removal	Ref.
$CuZnFe_2O_4$@N,S-doped BC (CZF@N,S-BC)	0.01	Hydrothermal	Beta vulgaris leaves	RB5	100	Dark	60	2	176.5	96.5	[63]
$MnFe_2O_4$@BC $ZnFe_2O_4$@BC	0.01	Coprecipitation	Chromolaena odorata roots	IC MB	70	Visible	120	7	173.47 129.91	94.83 98.60	[55]
P.harmala BC/Mn-$ZnFe_2O_4$	3.2	One-step pyrolysis	Peganum harmala plant	RhB	10	Dark	90	4	34.5	82	[69]
$ZnFe_2O_4$@BC	0.7	Single-step pyrolysis	Eucalyptus sawdust	RhB RBR	100 100	Visible	60	4.62	–	99.84 99.67	[71]
$ZnFe_2O_4$/Coffee ground residue BC	1.0	Coprecipitation	Coffee ground residue	MB	10	Visible	60	3	–	100	[79]
$ZnFe_2O_4$/Chitin BC	1.0	Coprecipitation	Chitin	PR MB	20 20	Visible	15 60	3	–	100	[80]
$ZnFe_2O_4$/ BC	0.5	Simple calcination method	Banana peels	MB	10	Visible	100	–	–	91.08	[72]
$ZnFe_2O_4$@AC	0.1	One-step carbonation activation	Cactus (*Opuntia stricta Haw.*)	RhB MO AY17	100	Dark	240	–	125.13 180.51 82.73	69 72 62	[73]
$ZnFe_2O_4$/Chitin BC	1.0	Sol-gel	Chitin	RhB	50	Visible	60	3	–	100	[60]
$ZnFe_2O_4$@ Waste Char (WC)	1.0	Wet in situ technique	corrugated paper and used face masks	RhB	10	Visible	70	7	25	92	[82]
$ZnFe_2O_4$@BC	0.5	One-pot thermal-calcination roasting	pomelo peel	MB	60	Visible	300	7	–	91	[81]
$ZnFe_2O_4$/BC	1.0	Coprecipitation	Chitin Residue	MB MO TZ	10	Visible	60	3	–	90 100 100	[83]

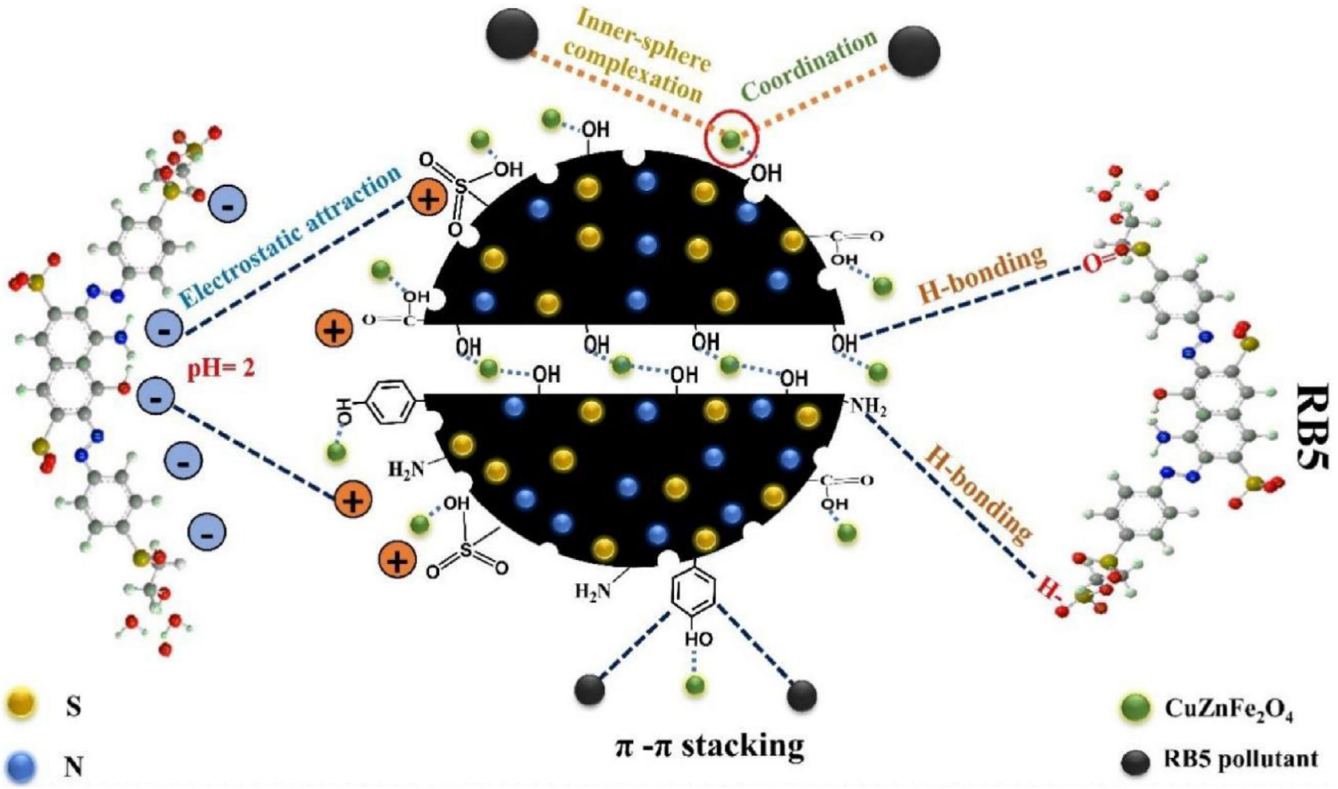

Figure 5. Adsorption mechanism of RB5 dye on CZF@N, S-BC composite.[63] Reproduced under the terms of the CC BY 4.0 license. Copyright 2024, Springer Nature.

degrade 100 ppm RhB dye under pH 4 within 60 min of visible light irradiation.[69]

$ZnFe_2O_4$ was supported by biochar derived from residues of coffee ground for the degradation of MB by photo-Fenton process. The biochar support to $ZnFe_2O_4$ does not only prevent aggregation of NPs but also ensures its uniform distribution over the surface. Pure $ZnFe_2O_4$ shows low photocatalytic activity and obtained degradation efficiency of only 38% within 60 min under visible irradiations due to rapid recombination of e^-/h^+ pairs, while the equivalent ratio of $ZnFe_2O_4$ and BC accounts for 100% degradation in the similar duration.[79] Similarly, authors have utilized chitin biochar to support $ZnFe_2O_4$ using coprecipitation method for degradation of ponceau red and MB dyes by identical photo-Fenton process. $ZnFe_2O_4$/BC nanocomposite was prepared by utilizing different mass ratios of $ZnFe_2O_4$ and biochar in order to decrease the electron recombination rate. The degradation mechanism of dyes relied on the generation of ROS radicals and interaction of dye pollutants with the surface of nanocomposite. The oxygen-rich functional groups in chitin biochar does not only accelerate the migration of photogenerated electrons at the surface of $ZnFe_2O_4$ but also reduces the e^-/h^+ pairs recombination.[80] In another study, similar approach was implemented, where chitin biochar was used to support $ZnFe_2O_4$ using sol-gel method for photocatalytic degradation of RhB dye by photo-Fenton process. The interaction of functional groups present on chitin biochar surface with $ZnFe_2O_4$ NPs does not only prevent aggregation but also reduces the band gap as well as the recombination rate of e^-/h^+ pairs. The mass ratio of $ZnFe_2O_4$ to BC certainly effect the photocatalytic activity of nanocomposite. For instance the higher amount of ferrite leads to the uneven or poor distribution over BC surface while the lesser amount might show the insufficiency in hydrogen peroxide activation leading to the decrease in photocatalytic activity. Therefore, the equivalent ratio of 1:1 of $ZnFe_2O_4$ to BC shows best photodegradation performance when 1.0 g/L employed to degrade 10 ppm RhB dye under visible light at pH 3 and 50 µL H_2O_2 within 20 min.[60] A single-step calcination method was employed to prepare $ZnFe_2O_4$/BC nanocomposite for the photocatalytic degradation of MB dye. Biochar derived from banana peels was incorporated in $ZnFe_2O_4$, enhances the visible light absorption while also inhibit e^-/h^+ pairs recombination. The photocatalytic degradation of 91.08% obtained for 10 ppm MB dye carried out using 0.5 g/L nanocomposite on exposure to visible light for 100 min. The photostability and significant photocatalytic activity of $ZnFe_2O_4$/BC nanocomposite was attributed to its superior band gap, enhanced specific surface area, higher active sites, and reduction in e^-/h^+ pairs recombination.[72] The one-step carbonization activation strategy was implemented to synthesize $ZnFe_2O_4$ loaded AC nanocomposite for the remediation of RhB, MO and AY-17 dyes.

The biowaste of *Opuntia Stricta Haw*. was utilized to derive biochar as well as magnetized AC and subjected to Box–Behnken Design (BBD)-response surface methodology (RSM) to optimize the dye adsorption process. The Elovich model provided the best fit for adsorption of RhB and AY-17 dye, which indicate a chemisorption mechanism, i.e. the adsorption rate decreases over time due to surface heterogeneity while the adsorption of MO followed the pseudo-second-order kinetics, suggesting that the rate of adsorption was influenced by the availability of adsorption sites and MO concentration. $ZnFe_2O_4$@AC shows higher adsorption efficiency for MO followed by RhB and AY-17 as predicted by Langmuir isotherm model, which determined maximum adsorption capacity of 180.51, 125.13, and 82.73 mg/g for MO, RhB, and AY-17 respectively.[73] Biochar derived pomelo peels was utilized for the synthesis of $ZnFe_2O_4$@BC composite using one-pot thermal-calcination method. The degradation of MB dye examined by photocatalysis as well as photo-Fenton process using photocurrent tests and UV-vis diffuse reflectance spectroscopy. The addition of H_2O_2 promotes the electron transfer while also inhibit the recombination of photogenerated electron-hole pairs. As an electron acceptor, H_2O_2 captured electrons from $ZnFe_2O_4$@BC and facilitate charge separation, result in higher photocurrent in $ZnFe_2O_4$@BC/H_2O_2 as compared to $ZnFe_2O_4$@BC system. The photo-Fenton degradation of MB dye performed by employing 0.5 g/L of $ZnFe_2O_4$/BC and 9 mM H_2O_2 to degrade 60 ppm MB under visible light within 180 min.[81] Sngle-step pyrolysis method was also employed to synthesize $ZnFe_2O_4$/Eucalyptus sawdust BC nanocomposite. Synergistic effect of adsorption and photo-Fenton degradation of RhB and reactive brilliant red X-3B (RBR) dyes by $ZnFe_2O_4$/BC nanocomposite represented in Figure 5. The removal efficiency of both dyes reaches up to 99% with the nanocomposite and H_2O_2 dosage of 0.7 g/L and 3 mmol/L respectively at a pH of 4.62 within 60 min. The photo-Fenton degradation of RhB and RBR dyes by $ZnFe_2O_4$@BC/H_2O_2 system involved the excitation of e^- to conduction band leaving photogenerated holes (h^+) in valence band.

$$ZnFe_2O_4 + hv \rightarrow ZnFe_2O_4(h^+ + e^-)$$

The e^- in conduction band reduces H_2O_2 to form $^\bullet OH$ while the h^+ in valence band oxidizes the H_2O as well as OH^- to produce $^\bullet OH$.

$$h^+ + H_2O \rightarrow H^+ + {}^\bullet OH$$

$$h^+ + OH^- \rightarrow {}^\bullet OH$$

$$H_2O_2 + e^- \rightarrow {}^\bullet OH + OH^-$$

The redox coupling of Fe^{+3}/Fe^{+2} e^- in $ZnFe_2O_4$ also enhance the activation of H_2O_2 to produce $^\bullet OH$ and $^\bullet OOH$ to degrade RB and RBR dyes[71] represented in Figure 6.

$$Fe^{3+} + e^- \rightarrow Fe^{2+}$$

$$Fe^{2+} + H_2O_2 \rightarrow Fe^{3+} + {}^\bullet OH + OH^-$$

$$Fe^{3+} + H_2O_2 \rightarrow Fe^{2+} + {}^\bullet OOH + H^+$$

4.2. Cobalt Ferrite/Biochar Nanocomposites

Cobalt ferrite has gained significant attention as a photocatalyst due to its sustainability, chemical stability, large saturation magnetization, and optical band gap of ~1.8 eV. The challenge of faster e^-/h^+ pair recombination can often mitigate by coupling of $CoFe_2O_4$ with biochar material that enhanced the charge separation. Table 3 summarizes the remediation of dye effluents by $CoFe_2O_4$/BC nanocomposites. Biochar derived from rice husk (RHB), sunflower husk (SHB) was used to support $CoFe_2O_4$ and nickel (II) doped cobalt (II) ferrite in single-stage in situ synthesis for the oxidative degradation of MO dye. The $CoFe_2O_4$@BC was utilized as a photo-Fenton catalyst to degrade MO dye. The photocatalytic degradation of MO was associated with the generation of $^\bullet OH$ and $^1O_2$ radicals from redox cycling of Fe^{+2}/Fe^{+3}. The degradation process employed 0.1 g/L $CoFe_2O_4$@BC with 3% H_2O_2 to degrade 40 ppm MO dye, result in 100% degradation by $CoFe_2O_4$/RHB within 120 min and $CoFe_2O_4$/SHB in 90 min under visible light.[84] In one of the study, $CoFe_2O_4$ modified with montmorillonite clay (MC) and starch for the removal of cationic dyes such as methyl violet (MV) and MB. The response surface methodology-central composite design (RSM-CCD) utilized to optimize various factors affecting the uptake process. The sorption efficiency of the MC/starch/$CoFe_2O_4$ nanocomposite was found to be significant, with more consistency observed with the pseudo-first-order kinetic model. The factors that influence the uptake process of MV and MB dyes include pH, temperature, time, dye concentration, and sorbent dosage. The significance of the solution pH identified as a key factor in the uptake process, affecting the process through ionization and changes in functional groups. Hence, the uptake process of MV and MB found to be increased with an increase in pH from 2 to 10. Several plausible mechanisms of adsorption represented in Figure 7. Among which pore saturation can be most effective due to porous structure of MC, starch and MC/starch/$CoFe_2O_4$ confirmed by BET and SEM analysis.[85]

Asif et al. biosynthesized four distinct ferrite/biochar nanocomposites for the adsorption of Blue-XGRR (Basic Blue 41) dye. The optimum conditions for the adsorption of dye were found in pH range from 10 to 11 using 50 g/L dosage of adsorbent with 60 min of contact time. The adsorption process follows pseudo second order kinetics and described well by Langmuir isotherms with maximum adsorption capacity of 46.90, 41.89, 35.33, and 25.09 mg/g for orange peels (OP)/$MnFe_2O_4$, peanut shells (PS)/$CuFe_2O_4$, tree twigs (TT)/$NiFe_2O_4$, and wood/$CoFe_2O_4$, respectively.[54] The AC derived from *Phoenix dactylifera* date stones was modified by $CoFe_2O_4$ using co-precipitation method for the sono-assisted adsorption of cationic dyes such as NB, MV and MB. The adsorption process follows pseudo-second-order kinetics and described well by Freundlich isotherm model and shows maximum adsorption capacity of 86.24, 83.90, and 87.48 mg/g for NB, MV and MB respectively. AC/$CoFe_2O_4$ nanocomposite shows excellent reusability unto ten adsorption-desorption cycles while the adsorption efficiency was reduced by only 6% even after seven times recycling.[74]

$CoFe_2O_4$@bio-carbon (CFBC) nanocomposites synthesized by co-hydrothermal and annealing method. The bio-carbon

Table 3. Comparative study of Cobalt ferrite/Biochar nanocomposites employed in adsorption and photocatalytic degradation of dye pollutants.

Catalyst	Catalyst dosage (g/L)	Synthesis method	Biochar feedstock	Dye	Initial dye conc. (ppm)	Light source	Reaction time (min)	pH	Adsorption capacity (mg/g)	% dye removal	Ref.
$CoFe_2O_4$/MC/starch	1.2	Coprecipitation	montmorillonite clay (MC) and starch	MV MB	10	Dark	60	8	43.95 47.51	99.45 98.67	[85]
$CoFe_2O_4$/OS	2.0 2.5	Coprecipitation	*Ocimum sanctum* plant (OS)	MB CV	10	Dark	60	10	200 100	86.34 73.75	[89]
$CoFe_2O_4$@BC	0.75	Co-hydrothermal and calcining	Apium	MB	10	Ozone	–	7	–	90.37	[75]
PBC/$CoFe_2O_4$/Mn-Fe-LDH	1.0	Coprecipitation	Pistachio biochar (PBC)	MB MO	10 10	Visible	50 50	2 2	–	94.5 83.75	[86]
$CoFe_2O_4$/bio-silica	0.67	Coprecipitation	Rice husk ash	MB	100	Dark	120	9	253.6	~99	[87]
Nickel (II)- cobalt (II) ferrite/BC	0.1	One-stage single reactor synthesis	Rice husk and Sunflower husk	MO	40	Visible	90	–		~100	[84]
g-C_3N_4/ $Ni_{0.1}Co_{0.9}Fe_2O_4$/ BC	0.5	Hydrothermal	Bamboo fiber	MB	20	Visible	120	–	–	96.7	[88]
Polyethyleneimine modified $CoFe_2O_4$/BC	–	Hydrothermal	Bamboo powder	CR	100	Dark	1440	6.5	435.9	96.2	[64]
Chitosan (CS)-$CoFe_2O_4$/BC	0.5	Cross-linked by glutaralde- hyde,	Waste cardboard	Amaranth MO	200	Dark	240	2 4	500.6 644	90 100	[90]
$CoFe_2O_4$/AC	3.0	Coprecipitation	*Phoenix dactylifera* date stones	MB MV NB	10	Dark	40	9 8 8	87.48 83.90 86.24	98.58 99.51 99.01	[74]
$CoFe_2O_4$/BC	0.4	Coprecipitation	*Ziziphus spina-christi* seeds	AO7	100	Sono-adsorption	15	7	–	98.5	[91]
$CoFe_2O_4$/BC	0.5	Hydrothermal	*Ulva lactuca L.*	CR	20	Visible	70	7	–	96	[78]
$CoFe_2O_4$/BC	1.0	Coprecipitation	*Eucalyptus* sawdust	DR80	25	UV	180	3	–	100	[92]
$CoFe_2O_4$/BC	0.1	Coprecipitation	*Chitin*	Ponceau	10	Visible	60	3	–	100	[93]

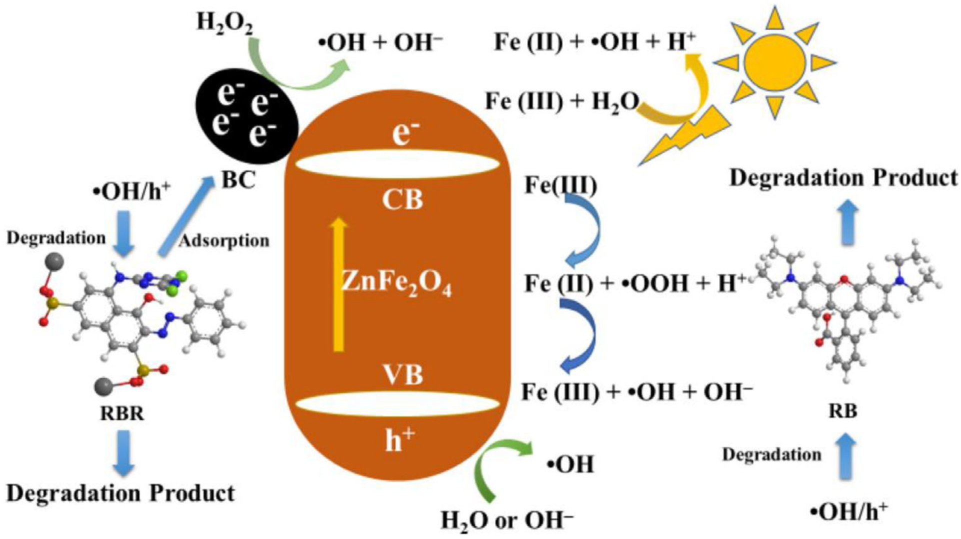

Figure 6. Synergistic adsorption and photo-Fenton degradation of RB and RBR dyes by $ZnFe_2O_4$/Biochar nanocomposite. Reproduced with permission from[71] Copyright 2024, Elsevier.

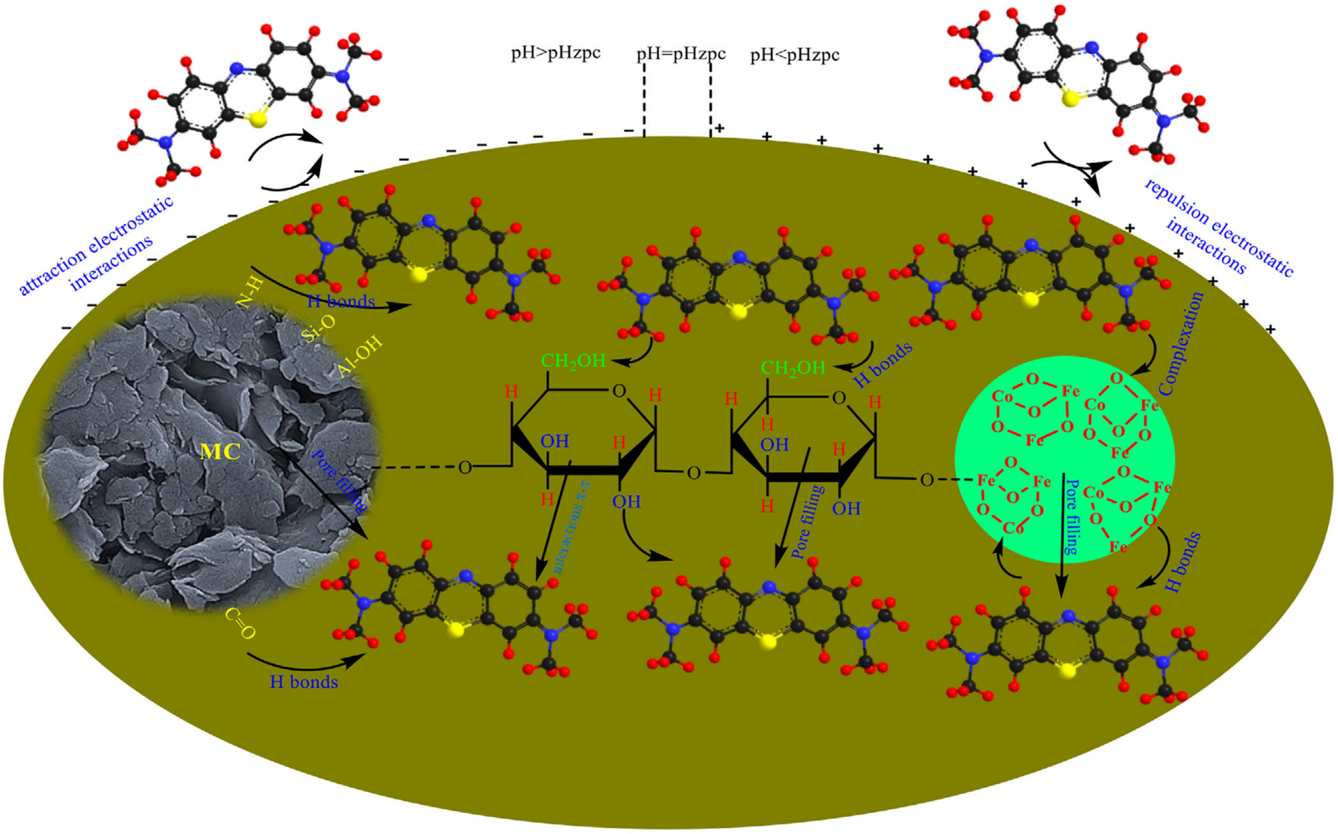

Figure 7. Adsorption mechanism of MB and MV dyes on MC/starch/$CoFe_2O_4$ nanocomposite. Reproduced with permission from[85] Copyright 2022, Elsevier.

nanoparticles derived from the apium stalks were decorated over CF-NPs to endow multi-adsorption mechanism for the removal of MB dye. CFBC nanocomposite possess higher specific area and porous surficial structure that maximize the removal of MB to 90.37% using 0.75 g/L adsorbent dosage at pH 7.[75] Zarei et al. fabricated a $CoFe_2O_4$/BC nanocomposite by simple co-precipitation strategy using $CoFe_2O_4$ magnetic NPs, pistachio biochar, and Mn-Fe-layered doubled hydroxide (LDH) for the photodegradation of cationic (MB) and anionic (MO) dyes. The photodegradation process was optimized using RSM by examining various factors such as catalyst dosage, dye concentration and reaction time. The exposure to UV excites the electrons on surface of $CoFe_2O_4$ and leads to the generation of electron-hole pairs while the biochar derived from pista-

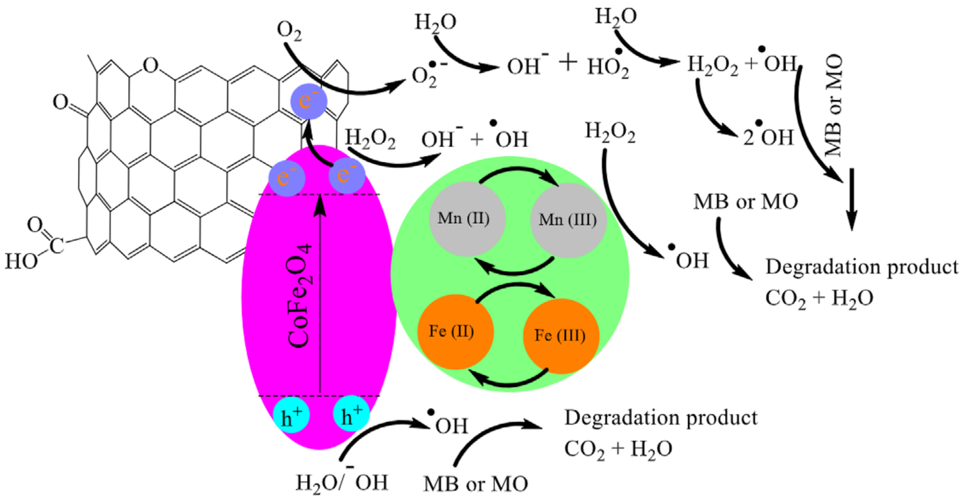

Figure 8. Photodegradation of MB and MO dyes using PBC/$CoFe_2O_4$/Mn-Fe-LDH photocatalyst. Reproduced with permission from[86] Copyright 2023, Elsevier.

chio shells (PBC) helps in trapping these electrons and delayed the electron-hole recombination. The Mn-Fe LDH also prevents the electron-hole pair recombination by creating type-II heterojunction, where photogenerated electrons get transferred from CB of $CoFe_2O_4$ to CB of Mn-Fe LDH while holes from VB of Mn-Fe LDH migrated to VB of $CoFe_2O_4$. These photogenerated electrons combined with dissolved O_2 in aqueous solution and generate $^{\bullet}O_2^{-}$. The superoxide radical further reacts with water to produce hydroxyl radicals ($OH^{\bullet}$). The holes in the VB also reacts with water molecules and generates $OH^{\bullet}$, further contributing to the degradation of dyes as shown in Figure 8. The photodegradation process carried out using 1.0 g/L of catalyst dosage to degrade 10 ppm of MB and MO achieved 99.10% degradation of MB and 99.89% of MO within 50 min at pH 10 and pH 2 respectively.[86] $CoFe_2O_4$ nanoparticle was incorporated into the matrix of biosilica (BSIL) extracted from rice husk using coprecipitation method for the adsorption of MB dye. The higher magnetic anisotropy and chemical stability of cobalt ferrite along with the higher active site's facilitation by silanol group synergistically affect the adsorption of MB dye. The deprotonation of silanol group with an increase in pH over the surface of $CoFe_2O_4$ interact MB dye molecules through electrostatic attraction and enhance the adsorption. The specific surface area and surface charge significantly influences the adsorption capacity of $CoFe_2O_4$/BSIL. The specific surface area of $CoFe_2O_4$/BSIL (283 m^2/g) was found to be much higher than BSIL (55 m^2/g) as determined by BET method, while the surface charge of BSIL was highly negative as compared to nanocomposite. As a result, $CoFe_2O_4$/BSIL nanocomposite exhibit maximum adsorption capacity of 253.6 mg/g, which was 5 times higher than BSIL (52.6 mg/g).[87] A heterojunction co-hybridized g-C_3N_4/$Ni_{0.1}Co_{0.9}Fe_2O_4$/biochar photocatalyst was fabricated using hydrothermal calcination method for effective photocatalytic degradation of MB dye. The photocatalytic degradation efficiency of 96.7% obtained by employing 0.5 g/L photocatalyst to degrade 20 ppm MB within 120 min on exposure to visible light. In this ternary photocatalyst, photogenerated electrons from g-C_3N_4 to $Ni_{0.1}Co_{0.9}Fe_2O_4$ transferred to the surface of biochar, results in enhancing the charge separation by reducing e^-/h^+ pairs recombination. These electrons react with H_2O_2 to produce $^{\bullet}OH$ radicals. Additionally H_2O_2 also reacted with $Ni_{0.1}Co_{0.9}Fe_2O_4$ to produce hydroxyl radicals and increases the photocatalytic efficiency.[88] Biochar derived waste bamboo powder was loaded on $CoFe_2O_4$ and modified by polyethyleneimine (PEI) for the adsorption of CR dye. The high adsorption capacity of PEI ascribed to the interaction of positively charged amino groups (generated by protonation) present in the main chain as well as in side branches with the negatively charged sulphate groups of CR dye. Hence, PEI modification of the magnetic biochar composite by impregnation method significantly enhances the adsorption capacity.

4.3. Copper Ferrite/Biochar Nanocomposites

Copper ferrites ($CuFe_2O_4$) nanoparticles have potential application in remediation of organic pollutants due to their magnetic properties, physical properties, and ease of separation using external magnetic field. $CuFe_2O_4$ nanoparticles known for the most effective visible-light sensitive photocatalyst. $CuFe_2O_4$ are highly efficient in sulphate radical-based advanced oxidation processes (AOPs) owing to its excellent stability and photocatalytic activity, high surface-to-volume ratio and low leaching rate of metals in degradation of dye pollutants. However, the ease of aggregation of $CuFe_2O_4$ nanoparticles reduces the availability of active sites, and thus prevented by supporting with biochar. Additionally, the oxygen-containing functional groups on the surface of biochar further interact with PS to generate ROS radicals and enhance the dye degradation. Table 4 illustrates various parameters involved in the removal of dye pollutants using $CuFe_2O_4$/BC nanocomposites.

Biochar derived from eucalyptus sawdust was utilized to synthesize $CuFe_2O_4$@Biochar nanocomposite using single-step sol-gel pyrolysis. $CuFe_2O_4$@BC utilized for PS-activation to degrade

Table 4. Removal of dye pollutants from industrial wastewater by $CuFe_2O_4$/BC nanocomposites.

Catalyst	Catalyst dosage (g/L)	Synthesis method	Biochar feedstock	Dye	Initial dye conc. (ppm)	Light source	Reaction time (min)	pH	Adsorption capacity (mg/g)	%Dye removal	Ref.
PS activated-$CuFe_2O_4$/BC	0.2	One-step sol-gel pyrolysis	Eucalyptus sawdust	MG	100	–	90	4	–	98.9	[94]
PS activated-$Cu_{0.9}Zn_{0.1}Fe_2O_4$@BC	0.2	Sol-gel	Eucalyptus sawdust	CV	50	–	60	5.1	–	96.9	[61]
$CuFe_2O_4$/BC	1.0	Sol-gel	malt bagasse	MB MO TZ	10 10 20	Visible	60	3	–	100 98 99	[58]
$CuFe_2O_4$/malt bagasse BC	1.0	Sol-gel	malt bagasse	RhB	10	Visible	60	3	–	88	[59]
$CuFe_2O_4$/Peanut shell	1.5	Coprecipitation	peanut shells	CV BBR	10 30	Dark	75	7.9	7.81 32.25	91.2 65.3	[95]

malachite green (MG) dye. The photodegradation of 100 ppm MG by employing 0.2 g/L $CuFe_2O_4$@BC and 0.25 mM of PS under 90 min of visible light irradiation achieved 98.9% degradation efficiency The increase in PS concentration from 0.1 mM to 0.25 mM generates higher sulphate radicals to active sites and enhances the degradation efficiency from 83.2% to 98.9%.[94] Zn-doped $CuFe_2O_4$@biochar composite was also fabricated using sol-gel pyrolysis method by Fan et al. to activate persulfate (PS) for degradation of CV dye. Zn doping certainly improves the photocatalytic activity of biochar supported $CuFe_2O_4$ by increasing crystallite size and saturation magnetization while also increases ratio of oxygen vacancies. These oxygen vacancies certainly accelerate the migration of electrons and generates ROS radicals for dye degradation. The optimal molar ratio of 1:9 of Zn to Cu in Zn-$CuFe_2O_4$@BC/PS shows the highest degradation of CV. The maximum degradation of 96.9% was observed when 0.2 g/L catalyst and 0.25 mM PS utilized at pH 5.1 to degrade 50 ppm CV dye.[61]

$CuFe_2O_4$ was supported on biochar derived from malt bagasse by sol-gel technique for the photodegradation of MB, MO, and TZ dyes under visible light. The photodegradation studies reveals that $CuFe_2O_4$ nanoparticles could only remove 50%, 47%, and 62% of MB, MO, and TZ, respectively. Further, the uniform dispersion of $CuFe_2O_4$ nanoparticles over biochar surface prevents the agglomeration and reduces the electron-hole pair recombination, which helps in improvement of photocatalytic activity. The band gap of pure $CuFe_2O_4$ (1.39 eV) was found to be decreased in $CuFe_2O_4$ supported biochar nanocomposite as 1.29 eV. This decrease in band gap allows the ease of electron migration from VB to CB and generate more ROS radicals for degradation of these dyes within 60 min under visible light.[58] In another study, Leichtweis et al. utilized similar composite as $CuFe_2O_4$:BC in 1:3 ratio (CFO1B3) for the degradation of RhB dye through photo-Fenton process. The pristine $CuFe_2O_4$ could only remove 39% of RhB dye under visible light within 60 min, whereas CFO1B3 efficiently removed ∼100% of 10 ppm and 50 ppm RhB dye within 10 min and 20 min. respectively on exposure to visible light.[59]

4.4. Manganese Ferrite/Biochar Nanocomposites

Manganese ferrite ($MnFe_2O_4$) stands out as soft magnetic ferrite with interesting properties of high permeability and strong magnetized saturation. The spinel ferrite ($MnFe_2O_4$) consists of Mn^{+2} ions occupying tetrahedral sites while Fe^{+3} ions occupied the octahedral sites. Table 5 represents $MnFe_2O_4$/BC nanocomposites employed for the adsorption and photocatalytic degradation of dye effluents from industrial wastewater. $MnFe_2O_4$ nanoparticles synthesized via co-precipitation technique was loaded over pinewood biochar by pre-treatment (MMNP-PrBC) and post-treatment (MMNP-PoBC) strategies for the adsorption of Eriochromie Black T (EBT) dye. The adsorption process employed 2.4 g/L adsorbent at pH of 7.5 for removal of 100 ppm EBT dye within 160 min. The adsorption capacity of 121.95 mg/g, found to be higher in MMNP-PoBC. The adsorption process followed

Table 5. Adsorption and Photocatalytic degradation of dye pollutants by $MnFe_2O_4$/Biochar nanocomposites.

Catalyst	Catalyst dosage (g/L)	Synthesis method	Biochar feedstock	Dye	Initial dye conc. (ppm)	Light source	Reaction time (min)	pH	Adsorption capacity (mg/g)	%Dye removal	Ref.
$MnFe_2O_4$@BC	2.4	Coprecipitation	Pinewood	EBT	100	Dark	160	7.5	121.95	97.8	[96]
$MnFe_2O_4$/PWF-BC	1.0	Hydrothermal	Poplar Wood flour (PWF)	RhB	20	Visible	60	5	–	93	[65]
$MnFe_2O_4$/BC	0.7	Hydrothermal	poplar wood	MB	20	Ultrasonic	20	5	–	99.8	[66]
$MnFe_2O_4$/OV	2.5 2.0	One-pot synthesis	*Origanum vulgare* (OV)	CV CR	10	Dark	90	7	14.59 34.45	43 72	[98]
NaOH-activated $MnFe_2O_4$@Zn-Al LDHs@Cellulose@AGBC	0.1	One-pot in situ	activated grapes stalks (AG)	MB	10	Dark	25	9	19.28	97.7	[97]
$MnFe_2O_4$/algae waste	0.5	–	*Scenedesmus obliquus*	MB CV	5 5	Dark	15	11	–	83 92.5	[99]
PMS activated-$MnFe_2O_4$/biochar (MX) (X=S, L, C)	0.05	Solvothermal	Corn stems (MS), Leaves (ML) Cores (MC)	Orange II	20	–	6	5.8	–	90 93 93	[100]
PDS activated-$MnFe_2O_4$/BC (KFS800)	0.2	Two-step hydrothermal	Fibrous bagasse	RhB	10	–	60	6.7	–	91.1	[101]
Zn-Al LDH-$MnFe_2O_4$-ESB-Starch	0.05	Coprecipitation	Egg-shell (ESB)	AB41	150	–	45	2	39.98	94.8	[102]
$MnFe_2O_4$/AV	2.0	Coprecipitation	*Alysicarpus Vaginalis* (AV)	CV	10	Dark	120	7	34.211	90	[103]
$MnFe_2O_4$@CPB	0.25	Coprecipitation	chitosan modified Biochar (CPB)	MO	10	Dark	150	3	134.9	99.5	[104]
$MnFe_2O_4$/SSMBC	1.0	Coprecipitation	Sewage Sludge magnetic biochar (SSMBC)	MB	40	Dark	1440	7	55.6	30	[105]
$MnFe_2O_4$@MOAC	1.0	Coprecipitation	*Moringa oleifera* activated carbon (MOAC)	RB4 IC AB158	100	Dark	40	3	32.45 33.53 35.27	86.35 90.45 92.65	[106]
$MnFe_2O_4$/BC	3.0	Coprecipitation	*Nigella Sativa* plant seeds (Black Cumin)	MB	10	Dark	45	10	10.07	99	[107]
Persulphate activated-$MnFe_2O_4$ carbon-based catalyst (CM-600)	0.4	One-pot thermal-calcination	Chitosan	AO7	50	–	30	6.5	–	99	[77]

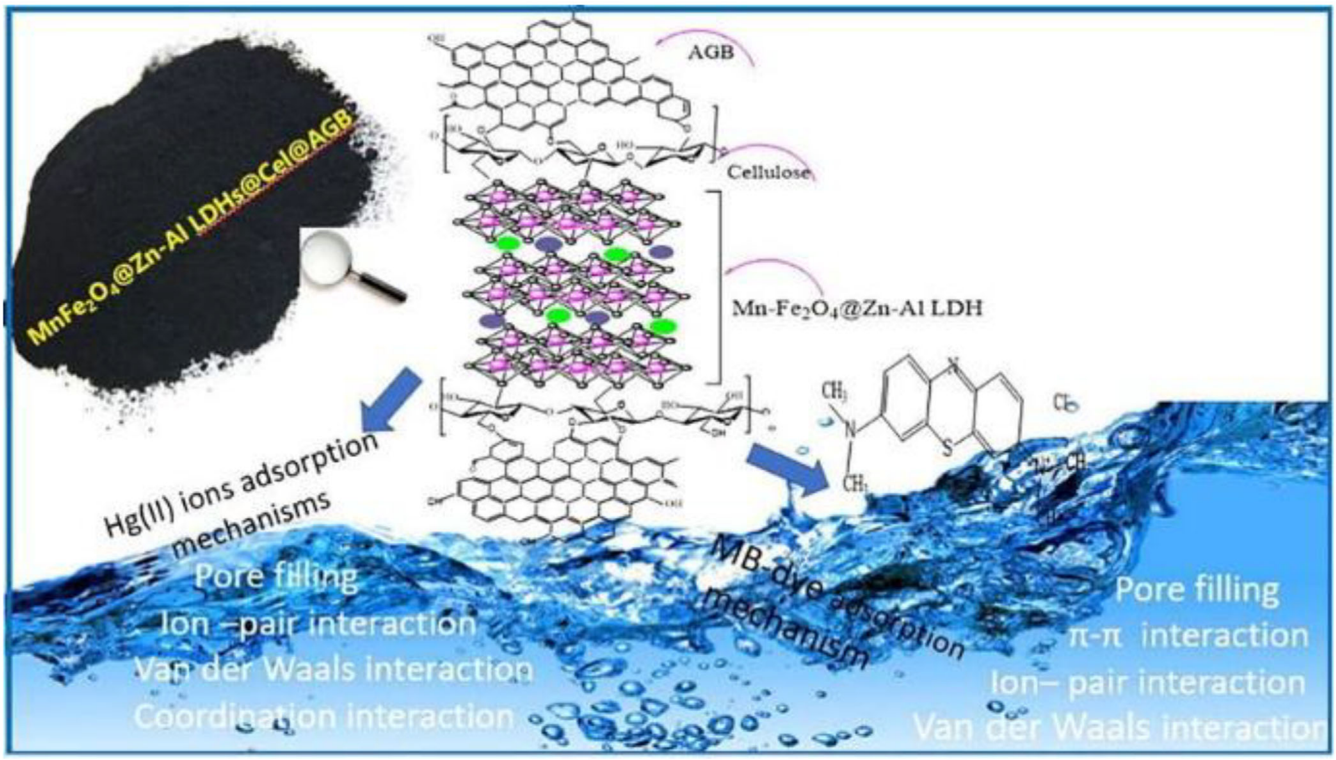

Figure 9. Adsorption of MB dye and Hg (II) ions by $MnFe_2O_4$@Zn-Al LDHs@Cel@AGB. Reproduced with permission from[97] Copyright 2021, Elsevier.

pseudo-second-order kinetics and described well by Langmuir isotherm model.[96]

Wood flour biochar (WFB) was used as a carrier to support $MnFe_2O_4$ (MFO) nanoparticles by single-step hydrothermal method for photo-Fenton degradation of RhB dye. The interaction of MFO nanoparticles with oxygen-containing functional group over WFB surface prevent its agglomeration and also enhances the specific surface area from 57.78 m^2/g (MFO) to 115.11 m^2/g (MFO/WFB). The activation of H_2O_2 by MFO catalyst further increases the RhB degradation. The photocatalytic degradation of 97.8% achieved for 20 ppm RhB using 1 g/L of MFO/WFB catalyst and 100 mM H_2O_2 at pH 5 on exposure to visible light within 60 min.[65] Biochar derived from poplar wood was also used as a carrier to support $MnFe_2O_4$ by hydrothermal method to degrade MB dye. The ultrasound-assisted heterogeneous Fenton-like process in photocatalytic degradation of MB generates ROS radicals by redox coupling of Fe(III)/Fe(II) and Mn(II)/Mn(III) while also enhances the mass transfer rate at solid-liquid interface.[66]

Mahmoud et al. designed a $MnFe_2O_4$/BC nanocomposites by fabricating $MnFe_2O_4$ nanoparticles with Zn-layered double hydroxide on cellulose and activated biochar derived from grapes stalks using in-situ method for the adsorption of of MB dye and Hg(II) ion from wastewater. The adsorption of MB primarily governed by van der Waals interactions and hydrogen bonding of MB molecules with surface functional groups of nanocomposite (such as –OH, –COOH, phenolic) and $\pi-\pi$ interactions between the aromatic carbon of MB and the graphitic domains of biochar. Alongside, the complexation and ion exchange between MB and functional groups on biochar and cellulose also contributed significantly to the adsorption process as shown in Figure 9. The adsorption process was governed by intraparticle diffusion mechanism and follows pseudo-second-order kinetics while best fitted in Freundlich isotherm model with maximum adsorption capacity of 19.28 mg/g and removal efficiency of 97.4%.[97] Among various AOPs, the sulphate-radical activated catalytic degradation has garner significant interest to researcher in recent years. The PS-activated catalytic degradation of AO7 dye by Du et al., utilizes chitosan-fabricated $MnFe_2O_4$ nanocomposite. The degradation of AO7 carried out by employing 0.4 g/L nanocomposite to degrade 50 ppm AO7 under pH 7, achieve 99% removal within 30 min. The degradation followed pseudo-first-order kinetics with a rate constant (k) of 0.14 min^{-1} higher than PS ($k = 0.0016$ min^{-1}) or unmodified $MnFe_2O_4$ ($k = 0.0019$ min^{-1}). The electron-transfer reaction of Mn^{+2}/Fe^{+2} with $S_2O_8^{2-}$ generated the $SO_4^{\bullet-}$ radicals which further produces $^{\bullet}OH$ radicals on hydrolysis. Alongside, the redox coupling between Fe^{+2}/Mn^{+2} and Fe^{+3}/Mn^{+3} also enhances the PS activation while also generate $^{\bullet}OH$.[77]

4.5. Nickel Ferrite/Biochar Nanocomposites

Nickel ferrite ($NiFe_2O_4$) has been featured as soft ferrimagnetic material with excellent chemical stability and low magnetic coercivity. The incorporation of $NiFe_2O_4$ into biochar enhances the adsorption efficiency by providing higher active sites to adsorb dye pollutants as well as ease of separation due to its magnetic property. Comparative studies of $NiFe_2O_4$/BC nanocomposites and various other ferrite/biochar nanocomposites employed for the adsorption and photocatalytic degradation of dye pollutants from wastewater are discussed in Tables 6 and 7 respectively. A ternary hybrid nanocomposite was fabricated by coupling biochar with Ag_3PO_4 and $NiFe_2O_4$ using hydrothermal method for photocatalytic removal of MB. The magnetic recoverability and photocatalytic activity of $NiFe_2O_4$ while higher specific surface area and presence of oxy/hydroxy functional groups on biochar surface produces synergistic effect in degradation of MB dye as well as for the adsorption of mercury. The dispersion of cubical structured Ag_3PO_4 and $NiFe_2O_4$ nanoparticles of size 200 nm and 500–1000 nm respectively over biochar surface revealed by SEM, enhances the surface area and number of active sites. BET analysis shows an increase in specific surface area from 11.27 m^2/g of pristine BC to 79.48 m^2/g of nanocomposite, shows mesoporous structure with average pore diameter of 140 nm for nanocomposite. Furthermore, the stability of Ag_3PO_4 improved on its addition to $NiFe_2O_4$/biochar in ratio 1:2, falling the band gap in visible region and enhances the photocatalytic activity. Upon exposure to visible light, electrons from valence band easily migrate to the conduction band due to narrow bandwidth of Ag_3PO_4 and $NiFe_2O_4$. The migration of electrons from CB of $NiFe_2O_4$ ($E_{CB} = 0.47$ eV) to the CB of Ag_3PO_4 ($E_{CB} = 0.56$ eV) while the transfer of holes from VB of Ag_3PO_4 ($E_{VB} = 2.83$ eV) to the VB of $NiFe_2O_4$ ($E_{VB} = 2.16$ eV) enhancing charge separation of e^-/h^+ pairs. Further, biochar traps the photogenerated e^- from $NiFe_2O_4$ and Ag_3PO_4 and preventing their recombination with holes in VB also helps in increasing the charge separation efficiency and ensures the higher generation of $O_2^{\cdot-}$ for photocatalytic degradation of MB as shown in Figure 10. The photocatalytic degradation of MB involved 2.6 g/L of nanocomposite, removing 94% MB within 90 min.[67] In another work, AC was generated from willow catkins by chemical activation method was loaded by $NiFe_2O_4$ to prepare nanocomposite using hydrothermal method for photodegradation of RhB dye. AC modified by 45 wt.% $NiFe_2O_4$ shows excellent photocatalytic activity due to an increase in oxygen vacancies which reduced the recombination of electron-hole pairs and enhances the charge separation efficiency. The photocatalytic degradation efficiency of 99.7% observed for 10 ppm RhB within 90 min on exposure to sunlight.[108]

5. Adsorption Mechanism

Adsorption has been widely recognized as the most efficient approach for the removal of dye effluents due to its cost-effectiveness, ease of operation, low-energy requirement, negligible, and high removal efficiency. The adsorption of dyes over MFBC nanocomposite is primarily governed by electrostatic interactions and the complexation of dyes with surface functional groups of MFBC. Additionally, both physiosorption and chemisorption driven by van der Waals forces and formation of chemical bonds between the contaminants and the surface functional groups play crucial roles in enhancing the overall adsorption capacity of MFBC nanocomposites. The exceptional physicochemical properties of MFBC nanocomposites, including its nanostructured morphology, high surface energy, extensive

Table 6. Comparative studies of Nickel ferrite/Biochar nanocomposites in removal of various dyes from industrial wastewater.

Catalyst	Catalyst dosage (g/L)	Synthesis method	Biochar feedstock	Dye	Initial dye conc. (ppm)	Light source	Reaction time (min)	pH	Adsorption capacity (mg/g)	%Dye removal	Ref.
$NiFe_2O_4/Ag_3PO_4$/BC (2:1:7)	2.6	Hydrothermal	Sugarcane	MB	10	Visible	60	7	241	94	[67]
Nickel ferrite (NF)/AC	1.0	Hydrothermal	AC derived from willow catkins (WC)	RhB	10	Visible	90	7		99.7	[108]
$MnFe_2O_4$/OPBC	1.0	Coprecipitation	orange peels (OP)	Basic Blue-XGRRL	100	Dark	60	11	46.90	45.40	[54]
$CuFe_2O_4$/PSBC			peanut shells (PS)					10	41.89	41.90	
$NiFe_2O_4$/TTBC			tree twigs (TT)					10	35.33	36.30	
$CoFe_2O_4$/WBC			Wood (W)					10	25.09	23.90	
Ni-$CoFe_2O_4$/Chitosan	0.6	Coprecipitation	Chitosan	GY-160	150	Dark	60	2	32.34	98.6	[109]
Zn-$NiFe_2O_4$/Starch			Starch						30.31		
$NiFe_2O_4$/AC	2.0	Hydrothermal	hazelnut shell	DR31	275	Visible	120	2	299.67	98.93	[110]
				DB78					209.13	99.27	
$NiFe_2O_4$/AC	0.3	Hydrothermal	*B. pilosa* (BP)	RhB	15	Dark	240	5.2	109.8	99.68	[111]
	0.3		weeds	MO	50		270	5.0	262.8	97	
	0.25			MR	30		180	6.0	248.5	99.5	

Table 7. Comparative studies of various MFBC nanocomposites used for the removal of dye effluents.

Catalyst	Catalyst dosage (g/L)	Synthesis method	Biochar feedstock	Dye	Initial dye conc. (ppm)	Light source	Reaction time (min)	pH	Adsorption capacity (mg/g)	%Dye removal	Ref.
Chitosan-crosslinked $BiFeO_3$/BC	2.0	Coprecipitation	Chitosan	MB	50	Dark	240	6	18.942	66.7	[112]
Zirconium ferrite/BC ($ZrFe_2O_5$-BC)	1.0	Hydrothermal Sulphuration	Wheat straw	RB19	60	Visible	300	2	127.99	88.82	[113]
$ZrFe_2O_5$/Wheat Straw BC	1.0	–	Wheat Straw	TZ	100	Visible	360	2	89.22 ± 0.31	89	[114]
($SrFe_{12}O_{19}$)/Sewage Sludge BC	2.0	Coprecipitation	Sewage Sludge	MG	500	Dark	40	7	388.65	77.73	[115]
$LaFeO_3$/BC/bi-sulfite (BS)	3.0	Sol-gel	Peanut Shell	MB	15	Visible	60	7	–	99.4	[62]
Chromium ferrite (CF)-BC	0.045	Coprecipitation	corn, rice, and wheat straw	CR	250	Dark	2500	2	582	92.29	[116]
$Ca_4Fe_9O_{17}$/BC	0.4	Coprecipitation	Egg shell (Ca precursor) Sawdust	MB RhB	40 40	Visible	36 36	7	–	99.4 99.2	[117]
$MgFe_2O_4$/C	0.05 0.05 0.2	Hydrothermal	AC {Opuntia stricta (catus)}	RhB MO AY17	30 40 40	Dark	180 240 240	3	90.08 158.12 96.49	–	[118]
$MgFe_2O_4$/BC	0.5	Coprecipitation	Jackfruit peel	MB MG	100	Dark	24 h	5	129.61 1238.30	–	[119]

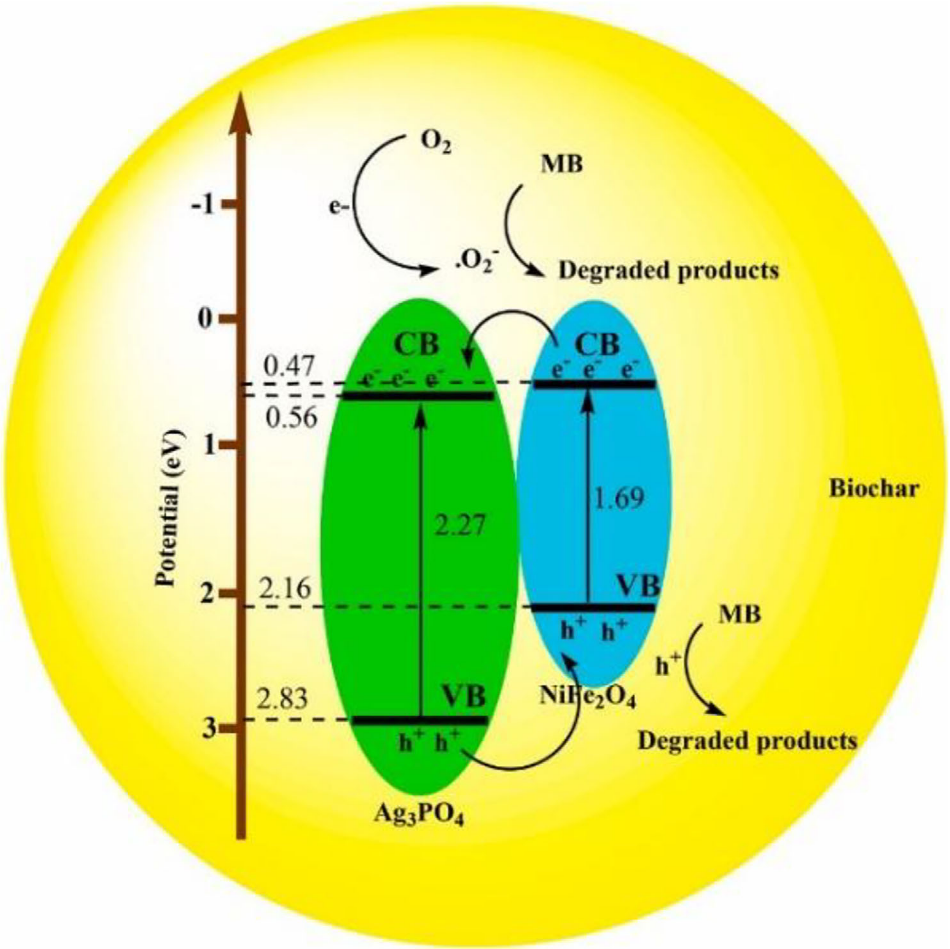

Figure 10. Photocatalytic degradation of MB dye using ternary $NiFe_2O_4$/Ag_3PO_4/Biochar nanocomposite. Reproduced with permission from[67] Copyright 2024, Elsevier.

specific surface area (SSA), and abundance of surface adsorption sites, significantly contribute to its superior adsorption performance. Furthermore, the synergistic effect between biochar and MFe_2O_4 nanoparticles enhances pollutant removal by providing additional active sites and improving the material's stability and reusability. The adsorption of cationic dyes such as MB and CV dyes over $MnFe_2O_4$–*Scenedesmus obliquus* composite occurred by synergistic effect of functional groups of algal biomass and glycine-functionalized $MnFe_2O_4$, via multiple interactions in the adsorption process. The biosorbent surface carries negative charges at pH $>$ PZC (point of zero charge: 7.6–8.7), facilitates strong electrostatic interactions with the positively charged MB and CV dyes. Further increasing in pH for, e.g., at pH 11, the negatively charged surface sites at algal biomass include carboxyl, phosphate, and hydroxyl groups also enhance dye adsorption. The dipole-dipole hydrogen bonding exists between O–H and N–H functional groups on the surface of composite with N-atoms of dye molecules. Also, the Yoshida H-Bonding involving interactions between O–H/N–H groups and the aromatic rings of MB and CV dyes, represented in Figure 11. The lone pair electrons of heteroatoms oxygen/nitrogen from the surface functional groups interact with the π-electrons of the aromatic rings in MB and CV account for n-π interactions. The intraparticle diffusion of dye molecules on the mesoporous composite structure with pore size 2–50 nm enhancing physisorption while the surface complexation of functional groups of sorbent with dyes enhancing the chemisorption.[99] In another study, the adsorption of RhB, MO, and MR dyes on $NiFe_2O_4$/AC composite. The adsorption of these dyes primarily governed by Pore-filling mechanism which involves the retention dye molecules within the porous matrix of the composite, based on the BET analysis that revealed high specific surface area of 993.5 m^2 g^{-1} and average pore diameter of 1.99 nm of $NiFe_2O_4$/AC composite. Alongside, the electrostatic interactions influenced by the pH-dependent surface charge of composite, which revealed that pH $<$ pH_{PZC} ($pH_azc \approx 6.4$) exhibits a positive surface charge that facilitates the adsorption of anionic dyes i.e., MO and MR dyes. Conversely, for pH $>$ pH_{PZC}, the negatively charged surface enhances the adsorption of cationic dye i.e., RhB. Additionally, the H–bonding between the oxy/hydroxyl-surface functional groups with dye molecules and π–π interactions between the sp^2-hybridized carbon of AC matrix with aromatic rings of dye molecules further stabilizes the adsorption process, represented in Figure 12.[111]

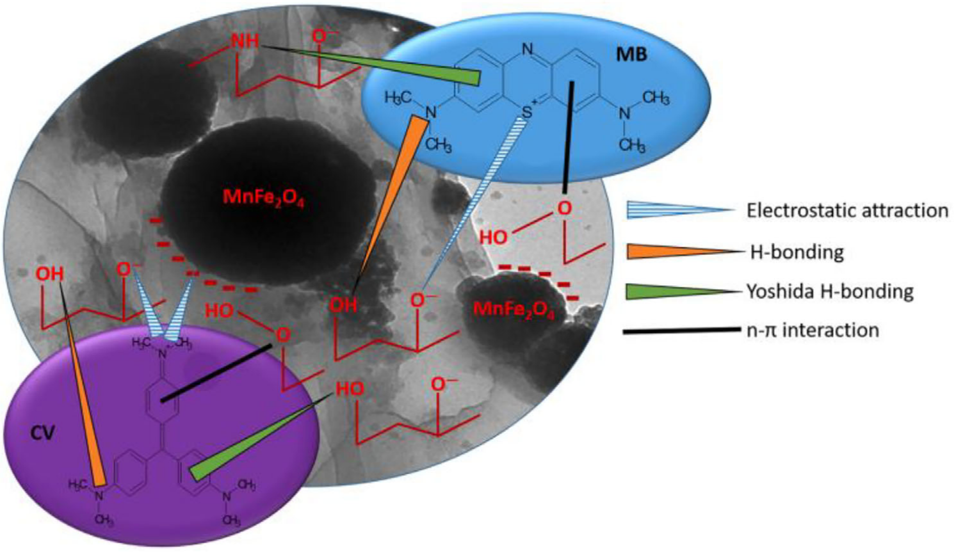

Figure 11. Possible mechanisms for the adsorption of MB and CV dyes on $MnFe_2O_4$–*Scenedesmus obliquus* composite. Reproduced with permission from[99] Copyright 2024, Elsevier.

6. Photocatalytic Degradation Mechanism

The photocatalytic degradation mechanism of organic pollutants involved various ROS radicals such as electrons, holes, hydroxyl, and superoxide radicals that degrade pollutants by redox reaction. Each of these reactive species plays significant role in degradation of dye pollutants. In photodegradation, when the incident photon energy equals to or less than the band gap of photocatalyst, the photogenerated electrons from the valence band (VB) migrate to the conduction band (CB). Further, the reaction of holes left behind in VB and electrons in CB band with water molecules in aqueous system will produced ROS radicals. The photocatalytic degradation primarily operates by generation of ROS radicals such hydroxyl ($^{\bullet}OH$), superoxide ($^{\bullet}O_2^{-}$), and sulphate ($SO_4^{\bullet-}$) to degrade complex dye molecules into simpler compounds.

$$\text{Dye effluents} + \text{ROS}\ \left(\bullet OH, \bullet O_2^{-}, SO_4^{\bullet-}, h^{+}, e^{-}\right)$$

$$\rightarrow \text{Intermediates} \rightarrow CO_2, H_2O$$

Among various AOPs, the sulphate radical-based peroxymonosulphate (PMS) activated system generates higher number of ROS over a wide pH range and improves degradation efficiency. PMS-activated systems are growing significant attention in AOP for degradation of dye molecules due to higher oxidation-reduction potential, selective reactivity and longer stability and lifetime. $CuFe_2O_4$@BC nanocomposite implemented as an efficient heterogeneous catalyst to activate persulphate ($S_2O_8^{2-}$) for the degradation of MG dye. The activation of PS through redox cycling of Cu and Fe species. Cu(II) and Fe(III) are reduced and oxidized in situ to produce highly reactive sulphate radicals ($SO_4^{\bullet-}$), hydroxyl radicals ($^{\bullet}OH$), and superoxide radicals ($O_2^{\bullet-}$). The PS could also react with H_2O and form HSO_5^{-} which reduces Cu(II) to Cu(I). Initially, Cu(II) oxidized to Cu(III) by $S_2O_8^{2-}$, generating $^{\bullet}SO_4^{-}$ radicals. However, Cu(III) further reacts to HSO_5^{-} to reduce back to Cu (II) and allowing the continuous redox cycling. While further reduction of Cu(II) to Cu(I) enhances the PS activation to yield $SO_4^{\bullet-}$ and OH^{-}. Electrons then transferred from Cu(I) to dissolved oxygen, subsequently reducing it to $O_2^{\bullet-}$.

$$\text{Cu (II)} + S_2O_8^{2-} \rightarrow \text{Cu (III)} + SO_4^{\bullet-} + SO_4^{2-}$$

$$\text{Cu (III)} + HSO_5^{-} \rightarrow \text{Cu (II)} + SO_5^{\bullet-} + H^{+}$$

$$\text{Cu (II)} + HSO_5^{-} \rightarrow \text{Cu (I)} + SO_4^{\bullet-} + OH^{-}$$

$$\text{Cu (I)} + S_2O_8^{2-} \rightarrow \text{Cu (II)} + SO_4^{\bullet-} + SO_4^{2-}$$

Similarly, Fe(III)/Fe(II) redox coupling with $S_2O_8^{2-}$ and HSO_5^{-} generates ROS.

$$\text{Fe (III)} + HSO_5^{-} \rightarrow \text{Fe (II)} + SO_5^{\bullet-} + H^{+}$$

$$\text{Fe (II)} + HSO_5^{-} \rightarrow \text{Fe (III)} + SO_4^{\bullet-} + OH^{-}$$

$$\text{Fe (II)} + S_2O_8^{2-} \rightarrow \text{Fe (III)} + SO_4^{\bullet-} + SO_4^{2-}$$

while Cu(I) and Fe(II) also react with $S_2O_8^{2-}$ and HSO_5^{-} to $SO_4^{\bullet-}$ and $^{\bullet}OH$ and also reduces the dissolved O_2 to produce $O_2^{\bullet-}$[94]

$$\text{Cu (I)} + O_2 \rightarrow \text{Cu (II)} + O_2^{\bullet-}$$

$$\text{Fe (II)} + O_2 \rightarrow \text{Fe (III)} + O_2^{\bullet-}$$

The biochar surface facilitated the electron transfer processes by the presence of oxygen-containing functional groups such as

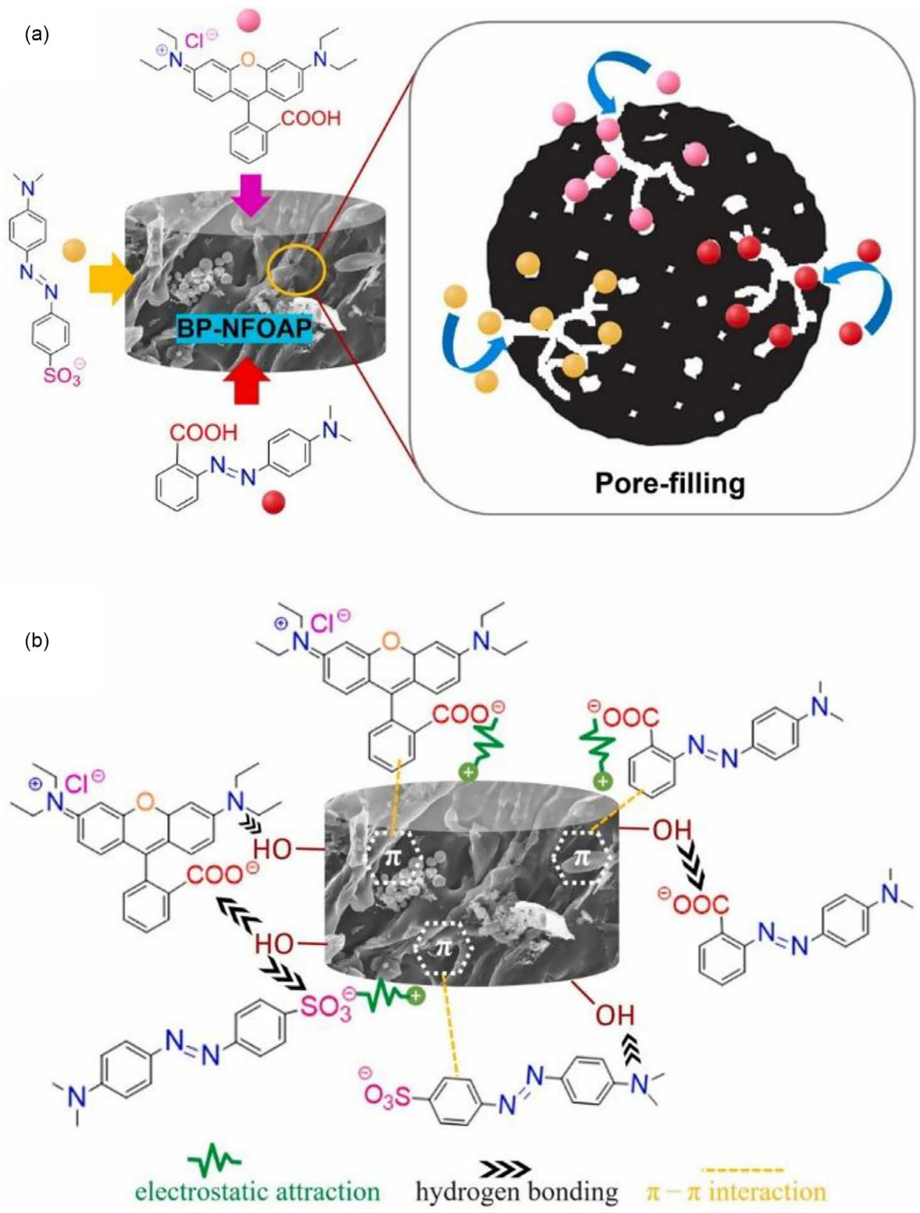

Figure 12. Different interactions such as a) pore-filling, b) electrostatic attraction, hydrogen bonding, and π–π interactions in adsorption mechanism of RhB, MO, and MR dyes with $NiFe_2O_4$/AC composite. Reproduced with permission from[111] Copyright 2025, Elsevier.

hydroxyl (−OH) and carbonyl (−C═O) can activate the PS system and could prevent $CuFe_2O_4$ agglomeration. The interaction of these functional groups generate $SO_4^{\bullet-}$ which further hydrolyzed to form $^{\bullet}OH$.

$$BC_{surface}-OOH+S_2O_8^{2-} \rightarrow SO_4^{\bullet-}+BC_{surface}-OO\bullet+HSO_4^{-}$$

$$BC_{surface}-OH+S_2O_8^{2-} \rightarrow SO_4^{\bullet-}+BC_{surface}-O\bullet+HSO_4^{-}$$

$$SO_4^{\bullet-}+H_2O \rightarrow \bullet OH+SO_4^{2-}+H^{+}$$

The MFe_2O_4/BC-PMS systems have great potential in generation of additional ROS such $^1O_2$ and $^{\bullet}O_2^{-}$ along with $SO_4^{\bullet-}$ and $^{\bullet}OH$, results in enhanced degradation of dye pollutants. For instance, the development of $MnFe_2O_4$-loaded graphitized hierarchical porous biochar ($MnFe_2O_4$/MS) for the activation of PMS by Fu et al., paved an excellent pathway for utilization of corn-based biochar with MFe_2O_4 to degrade Orange-II dye. The degradation mechanism follows both radical and nonradical pathways. The radical-induced pathway involved the PMS activation to generate $^{\bullet}SO_4^{-}$ and $^{\bullet}OH$ over the surface of $MnFe_2O_4$ nanoclusters that provide the active sites while graphitized porous biochar matrix enhances electron transfer reactions mediated by redox coupling of Mn(II)/Mn(III) and Fe(II)/Fe(III).

$$Mn\,(II)+HSO_5^{-}- \rightarrow Mn\,(III)+{}^{\bullet}SO_4^{-}+OH^{-}$$

$$Mn\,(III)+HSO_5^{-} \rightarrow Mn\,(II)+\bullet SO_5^{-}+OH^{-}$$

$$\text{Fe (III)} + \bullet O_2^- \rightarrow \text{Fe (II)} + O_2$$

$$\text{Fe (II)} + HSO_5^- \rightarrow \text{Fe (III)} + {}^{\bullet}SO_4^- + OH^-$$

Further $^{\bullet}SO_4^-$ can react with OH^-/H_2O to form $^{\bullet}OH$ while SO_5^{2-} hydrolyzed to form $\bullet O_2^-$. The formation of $^{\bullet}O_2^-$ also influenced by PMS decomposition and also in reduction of Fe(III) to Fe (II) and sustaining the redox cycle. The nonradical pathway involved the generation of singlet oxygen ($^1O_2$) by self-decomposition of PMS, promoted by C═O functional groups on the biochar surface while graphitized biochar matrix mediated electron transfer from dyes (electron donors) to PMS (electron acceptor) further enhances the degradation of Orange-II dye molecules.[100]

$$SO_5^{2-} + H_2O \rightarrow \bullet O_2^- + SO_4^{2-} + H^+$$

$$^{\bullet}SO_4^- + H_2O \rightarrow SO_4^{2-} + HSO_4^- + \bullet\, OH + H^+$$

$$HSO_5^- + SO_5^{2-} \rightarrow SO_4^{2-} + HSO_4^- + {}^1O_2$$

The magnetic $MnFe_2O_4$-decorated graphite-like porous biochar (KFS800) nanocomposite utilized to activate peroxydisulfate (PDS) for degradation of RhB dye. The redox coupling of Mn(II)/Mn(III) and Fe(II)/Fe(III) activate PDS to generate ROS, such as $SO_4^{\bullet-}$, $^{\bullet}OH$, $^{\bullet}O_2^-$, and $^1O_2$ radicals. Alongside, the oxygen-containing surface functional groups on KFS800 also activate PDS and generate $SO_4^{\bullet-}$.

$$\text{Mn (II)} + S_2O_8^{2-} \rightarrow \text{Mn (III)} + SO_4^{\bullet-} + SO_4^{2-}$$

$$\text{Fe (II)} + S_{2O_8}^{2-} \rightarrow \text{Fe (III)} + SO_4^{\bullet-} + SO_4^{2-}$$

$$(MnFe_2O_4/KFS800)\quad -OH + S_2O_8^{2-} \rightarrow HSO_4^- + SO_4^{\bullet-} \\ + (MnFe_2O_4/KFS800) - O^{\bullet}$$

The degradation mechanism involved the free radical pathway where $^{\bullet}OH$ radicals generated by $SO_4^{\bullet-}$ on reaction with H_2O/OH^- while $S_2O_8^{2-}$ react with H_2O to produce superoxide radicals $O_2^{\bullet-}$, whereas the nonradical pathway involved the generation of singlet oxygen $^1O_2$ from $O_2^{\bullet-}$ under acidic (H^+) and alkaline conditions (OH^-)[101] as shown in Figure 13.

$$SO_4^{\bullet-} + H_2O/OH^- \rightarrow HSO_4^-/SO_4^{2-} + \bullet\, OH$$

$$S_2O_8^{2-} + H_2O \rightarrow SO_4^{\bullet-} + O_2^{\bullet-} + H^+$$

$$\bullet O_2^- + H^+/OH^- \rightarrow {}^1O_2 + OH^-$$

$MnFe_2O_4$@BC utilized as heterogenous Fenton-like catalyst for the activation of H_2O_2 to degrade RhB dye, The generation of ROS such as hydroxyl radicals ($^{\bullet}OH$) and superoxide radicals ($^{\bullet}O_2^-$) was facilitated by the redox cycling of $\equiv Fe^{2+}/\equiv Fe^{3+}$ and $\equiv Mn^{2+}/\equiv Mn^{3+}$. The higher reduction potential of $\equiv Mn^{3+}/\equiv Mn^{2+}$ (1.51 V) compared to $\equiv Fe^{3+}/\equiv Fe^{2+}$ (0.77 V) facilitate the electron transfer from $\equiv Fe^{2+}$ to $\equiv Mn^{3+}$, that further regenerate the active sites $\equiv Fe^{2+}$ and $\equiv Mn^{2+}$. The porous structure of wood flour biochar (WFB) prevents aggregation of $MnFe_2O_4$ nanoparticles, while the $\pi-\pi$ interactions and oxygen-containing functional groups in WFB facilitate the migration of electrons and ensure in stabilizing the redox cycling of Mn and Fe.[65] The synergistic potential of ultrasound-assisted heterogeneous Fenton-like system employed to degrade MB dye using $MnFe_2O_4$/biochar nanocomposite.[66] The redox coupling of Fe(III)/Fe(II) and Mn(III)/Mn(II) to activate hydrogen peroxide (H_2O_2) for generation of highly ROS; $^{\bullet}OH$ and $^{\bullet}O_2^-$. The reduction of Fe(III) to Fe(II) by H_2O_2 generates $HO_2^{\bullet}$, which further dissociate to $^{\bullet}O_2^-$ while H_2O_2 oxidized Mn(II) to Mn (III) generate $^{\bullet}OH$. Furthermore, $HO_2^{\bullet}$ also generate $^{\bullet}OH$ by reaction with H_2O_2, represented in Figure 14. The ultrasonic irradiation generates $^{\bullet}OH$ by dissociation of H_2O_2 and H_2O while also promotes cavitation and increases surface area to 95.1 m^2/g from 41.4 m^2/g to further enhances the production of ROS. In another study, the degradation of MB by $ZnFe_2O_4$@BC involved a synergistic effect of visible light-driven photocatalysis and Fenton-like process. The photogenerated e- in CB react with O_2 to produce $^{\bullet}O_2^-$ while the holes (h^+) oxidized H_2O to $^{\bullet}OH$.

7. Factors Affecting Adsorption and Photocatalytic Degradation

The photocatalytic degradation and adsorption process of dyes can be affected several operational parameters including MFBC catalytic system, catalyst loading, dye concentration and pH as shown in Figure 15. In order to ensure the efficient degradation of dye pollutants, these parameters need to be optimized for instance by implying RSM considering the regeneration capability and reusability of MFBC nanocomposite.

7.1. Effect of Adsorbent/Catalyst Dose

The photocatalyst amount significantly influences the photocatalytic activity of MFBC nanocomposite. The increasing of catalyst dosage often results in higher photocatalytic activity due to increase in number of active sites for the adsorption of pollutants, while also lead to the generation of ROS radicals responsible for degradation of pollutants. For instance, the increase in catalyst dosage from 0.3 g/L to 0.7 g/L, significantly improved MB degradation efficiency to 99.8% within 20 min, due to higher availability of active sites. However, further increase in catalyst loading to 1.2 g/L decreases the degradation efficiency to 89.9%, as excessive catalyst scavenges $^{\bullet}OH$ by Fe^{2+}[66] In another study, the increase of $ZnFe_2O_4$/BC dose from 0.5 g/L to 1.0 g/L improved the photodegradation efficiency from 68% to 100%. However, further increasing of $ZnFe_2O_4$/BC dosage to 2.0 g/L, i.e., beyond the optimal value of 1.0 g/L reduces the photocatalytic activity due to the aggregation of nanoparticles that

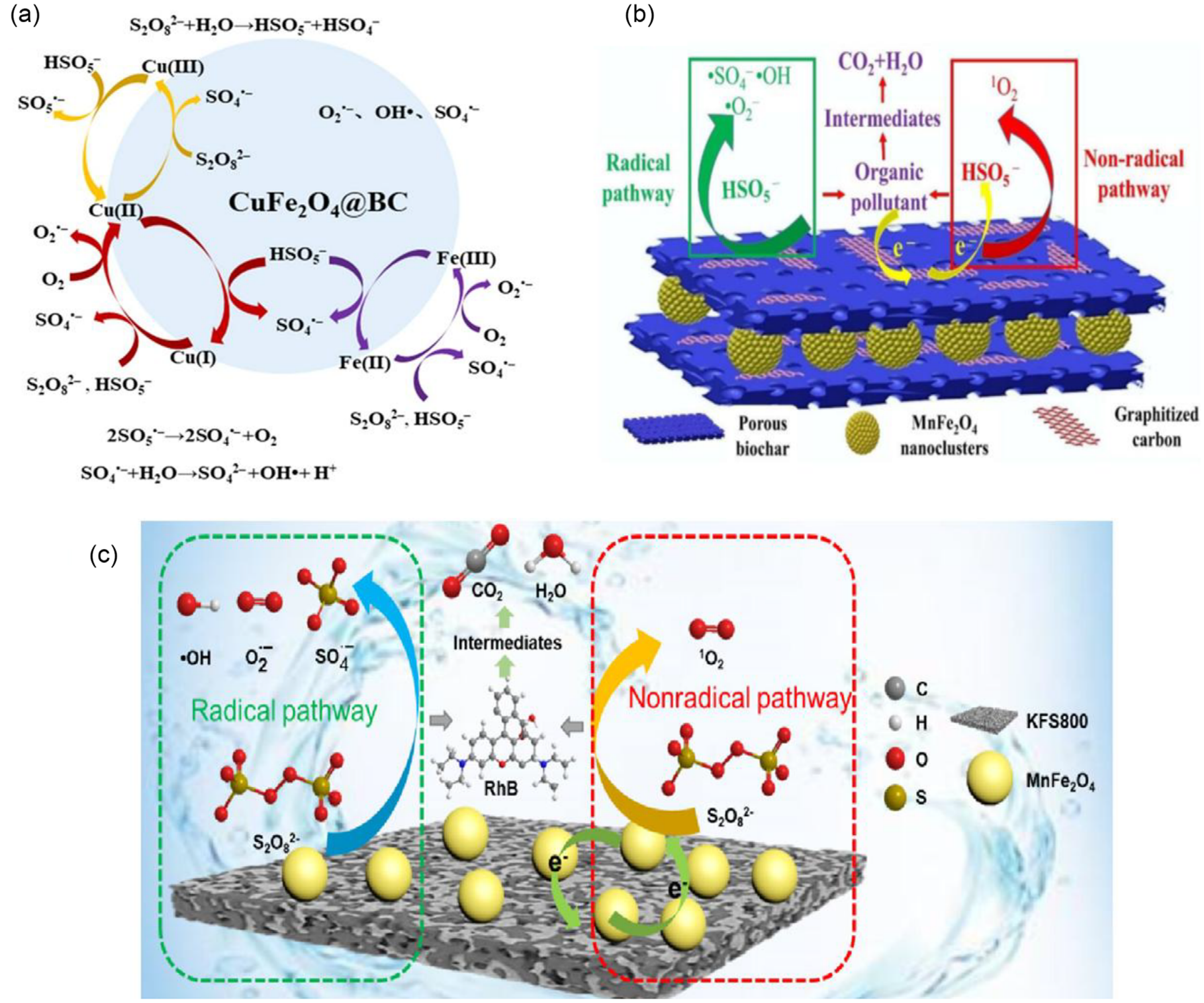

Figure 13. a) $CuFe_2O_4$@biochar/PS system for degradation of malachite green dye. Reproduced with permission from[94] Copyright 2021, Elsevier. b) PMS activated-$MnFe_2O_4$/graphitized hierarchical porous biochar for degradation of Orange-II dye. Reproduced with permission from[100] Copyright 2019, Elsevier. c) PDS-activated $MnFe_2O_4$–decorated Graphite-Like Porous Biochar (KFS800) heterogeneous catalyst for degradation of RhB dye.[101] Reproduced under the terms of the CC-BY-NC-ND 4.0 license. Copyright 2024, ACS Omega.

reduces the specific surface area as well as scattered the irradiations required for catalyst activation, hence decreases overall photocatalytic efficiency.[79]

7.2. Effect of Dye Concentration

The adsorption and photocatalytic degradation of dyes largely influenced by the initial dye concentration. As the dye concentration affects both, removal efficiency as well as the adsorption capacity. The lower concentration of dye effluents leads to better interaction of dye pollutants with the active sites on photocatalyst surface and achieves higher removal efficiency. The photocatalytic degradation efficiency also affected by the generation of ROS radicals such OH, hence in case of higher pollutant concentration, the light irradiation often largely absorbed by the dye pollutants, restricting it's reach to the photocatalyst surface and thus lowers the production of ROS, reducing the removal efficiency by MFBC nanocomposite.

7.3. Effect of pH

The pH of a solution can significantly affects the photocatalytic degradation efficiency by influencing catalyst's surface charge, dye ionization, and interaction of functional groups on the active sites. For instance, the removal of RB5 dye by $CuZnFe_2O_4$@N,S-doped biochar nanocomposite was assessed within the pH range from 2 to 11. Zeta potential analysis revealed that the CZF@N,S-BC composite's surface charge changes with pH, peaking at 32 mV (pH 2) and reaching −25.3 mV (pH 11), while the pH_{PZC} was found to be 5.3. For pH < pHpzc, i.e., at acidic pH (i.e., pH 2), the adsorption capacity of 176.50 mg/g was observed for RB5 with removal efficiency of 81.1% which can attributed to

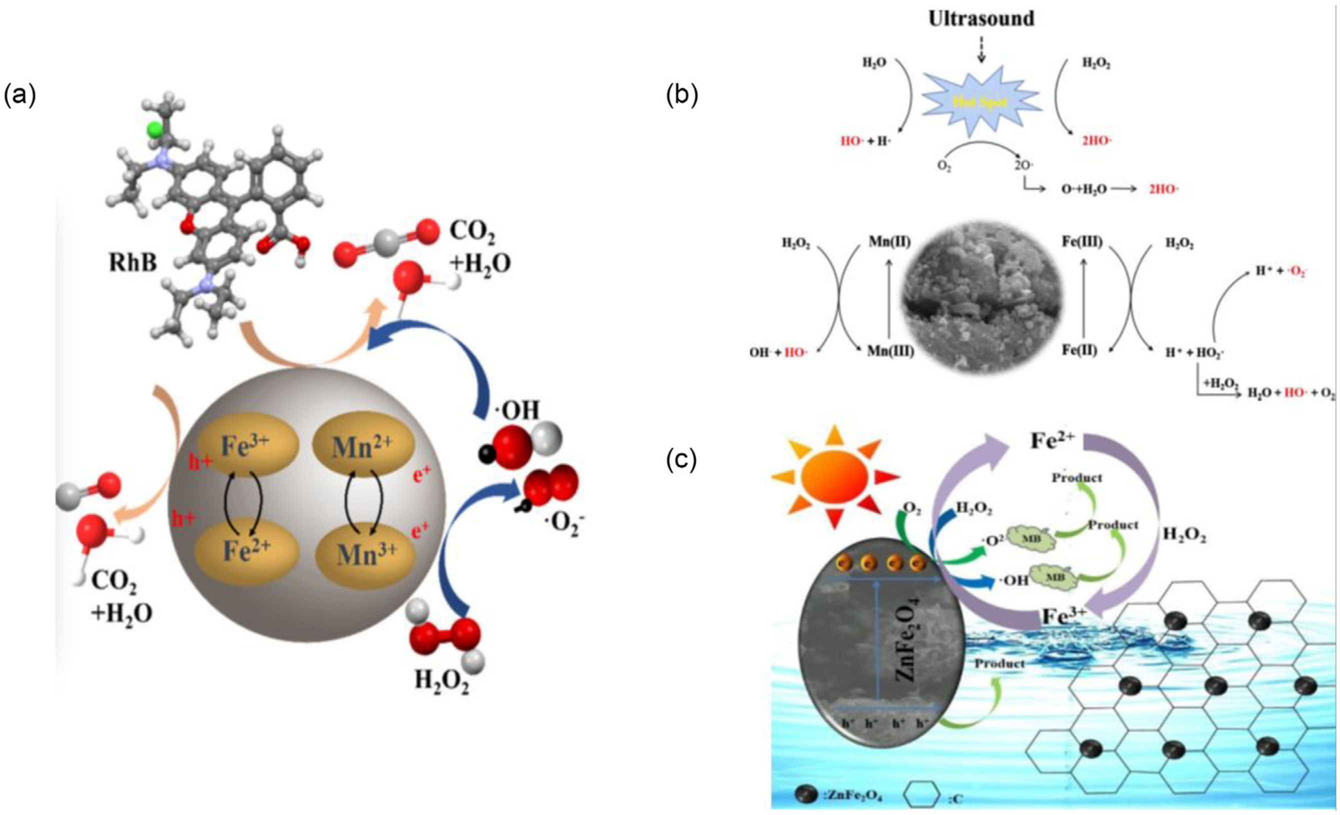

Figure 14. a) Degradation of RhB dye by H_2O_2 activated-MFO-WFB nanocomposite. Reproduced with permission from[65] Copyright 2021, Elsevier. b) Ultrasound-assisted heterogeneous Fenton-like process for degradation of MB using $MnFe_2O_4$/BC. Reproduced with permission from[66] Copyright 2021, Elsevier. c) Proposed mechanism for MB dye degradation by $ZnFe_2O_4$@BC nanocomposite. Reproduced with permission from[81] Copyright 2024, John Wiley and Sons.

the strong electrostatic interaction between positively charged CZF@N,S-BC surface with negatively charged SO_3^- of RB5 dye molecules. While at pH > pHpzc, i.e., for pH 11, the adsorption capacity gradually decreased to 46.51 mg/g with removal efficiency of 23.25% results due to the interfering of OH^- ions at the binding sites.[63] In another study, the removal of MB dye using heterogenous Fenton-based $MnFe_2O_4$/BC nanocomposite was studied in the pH range from 3 to 11. The degradation efficiency initial increases from 91.2% to 99% by varying pH from 3 to 5, but further decreases to 68.8% on increasing pH from 5 to 11. Under highly acidic conditions (pH 3), the presence of excess H^+ ions suppressed hydroxyl radical activity. While in alkaline conditions (pH 9–11), the formation of iron hydroxide precipitates and the accelerated decomposition of H_2O_2 limited the production of ROS radicals.[66]

7.4. Effect of H_2O_2

The advanced oxidation process of catalytic dye degradation, such as Fenton and Photo-Fenton, the generation of hydroxyl radicals ($^{\bullet}OH$) from H_2O_2 has been crucial for achieving higher degradation efficiency. However, beyond an optimal concentration, i.e., the higher H_2O_2 concentration may lead to decrease the degradation efficiency due to radical quenching. For e.g the ultrasonic assisted photo-Fenton degradation of MB using MFBC nanocomposite shows an increase in degradation efficiency from 26.5% to 99% on increasing the H_2O_2 concentration from 0 mM to 15 mM within 20 min. However further increase in H_2O_2 amount to 25 mM decreases the degradation efficiency to 81.1% due to scavenging effect of H_2O_2.[66]

8. Regeneration, Stability, and Reusability of MFBC Nanocomposites

8.1. Stability and Reusability

Stability and reusability often considered to determine the economic viability and sustainability of MFBC nanocomposite in removal of dye pollutants from wastewater. Stability of nanocomposite moreover refers to the efficiency of MFBC in effective removal of dye effluents without loss of structural integrity, surface morphology, and accessibility to active sites when subjected to repeated cycle of adsorption and photocatalytic degradation with variation in pH, catalyst load, and temperature. The tendency of aggregation of metal ferrites may results in decreasing of active sites, however the biochar support helps in reducing the agglomeration and uniform dispersion that enhances the specific surface area as well as active sites for adsorption and photocatalysis. In recent times, Spinel ferrites widely explored as a heterogeneous catalyst for activation of PMS in generation of ROS for degradation of dye pollutants.

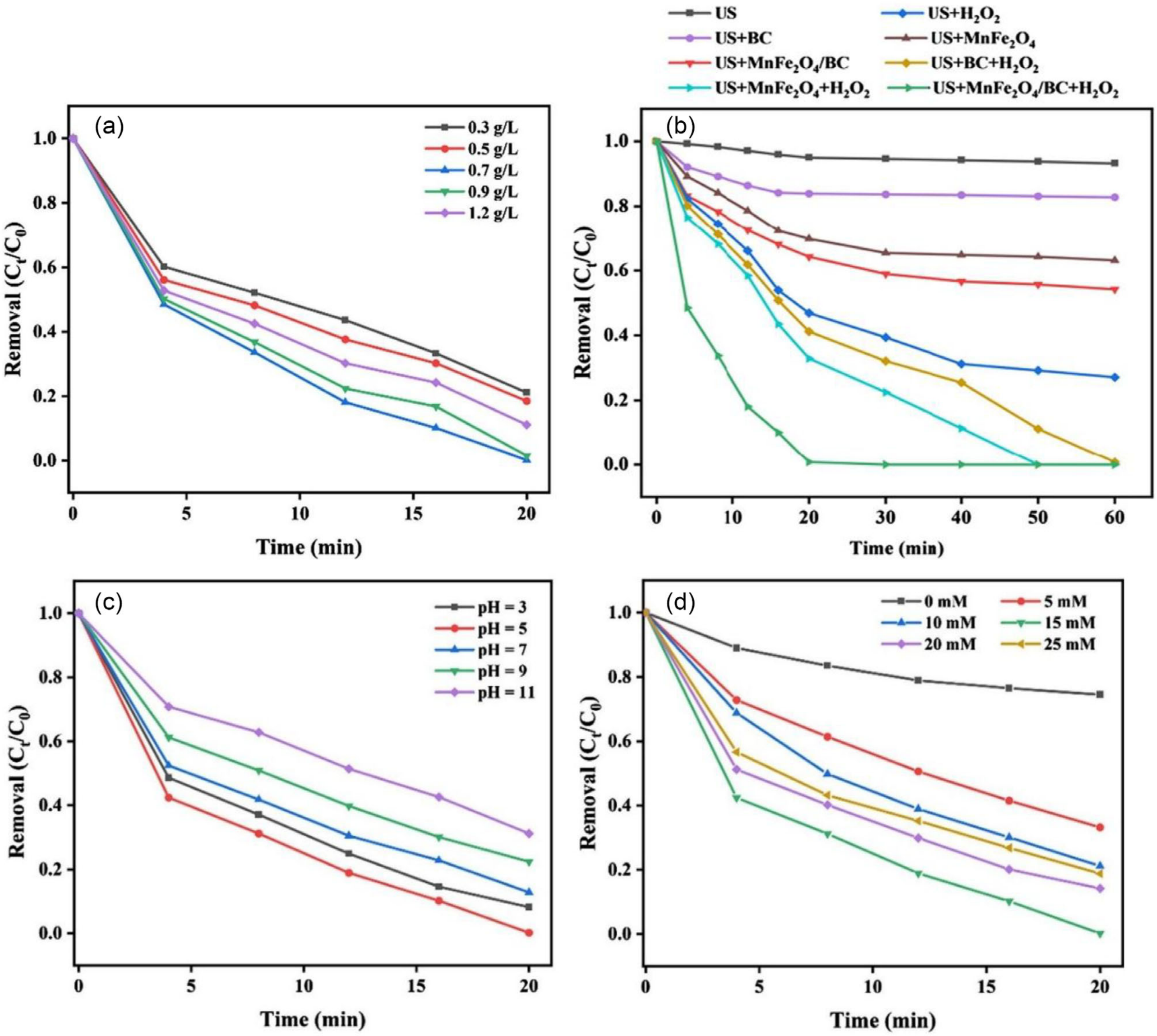

Figure 15. Ultrasound assisted Photo-Fenton degradation of MB using different a) catalyst load, b) catalytic systems, c) initial pH, d) H_2O_2 concentration, (MB concentration = 20 ppm). Reproduce with permission from[66] Copyright 2021, Elsevier.

However, under oxidative or acidic conditions, the leaching of metal ions of MFe_2O_4 leads to undermine the catalyst stability and reusability and poses significant eco-toxicological risks. To address this issue, MFe_2O_4 integrated into biochar matrix to form nanocomposite. The biochar support to MFe_2O_4 immobilizes the nanoparticles preventing their aggregation and leaching while facilitates electron transfer during PMS activation. The biochar also offers a high surface area and porosity, enhancing the active sites for adsorption and photocatalytic degradation. The reusability of nanocomposite determined by its efficiency in removal of pollutants over multiple cycles.

8.2. Regeneration

Regeneration of MFBC nanocomposites accounts for the practical applicability and its effective performance in removing dye effluents from wastewater. The performance of these composites often evaluated by the retention of adsorption capacity and photocatalytic activity and also the availability of active sites even after repeated adsorption and desorption cycles. Enhancing regenerability reduces operational cost and minimizing environmental impact in implementation of MFBC nanocomposites for large-scale wastewater treatment. The utilization of pure biochar in dye wastewater treatment raises a concern of limited adsorption efficiency as well as difficulty in post-treatment recovery. The metal ferrite modified biochar shows excellent photocatalytic activity in presence of visible light and characteristic magnetic property account for easy recovery. More often, the challenges associated with the chemical and thermal stability of MFBC nanocomposites on exposure to acidic or alkaline eluents affects the adsorption efficiency. To overcome such challenges, controlled synthesis of MFBC nanocomposites that involve surface functionalization, doping or formation of hetero-structures enhance the stability, and high surface activity.

Additionally, the regeneration efficiency is also determined by the extent to which desorption restores both the active sites as well as the porous architecture of the biochar matrix. Repeated regeneration cycles may lead to pores blockage or leaching of metal ferrites nanoparticles and gradually decreases the adsorption capacity. The reusability and regeneration capacity of MFBCs are critical factors in determining their techno-economic feasibility in wastewater treatment. High regeneration efficiency decreases the need for pristine adsorbents, reduces overall treatment costs, and mitigates the environmental impacts associated with adsorbent disposal.

9. Conclusions and Future Prospects

The rapid industrial expansion intensified the generation of waste as well as the exploitation of natural resources leading to environmental and water pollution. This review article discusses the recent advancement in wastewater treatment methods focused on mitigating the adverse impact of dye pollutants through an eco-friendly and sustainable approaches. The conversion of waste biomass from agricultural and forestry activities into biochar through pyrolysis reflects a key idea in sustainable waste management by reducing landfill volumes, diversion of organic waste from incineration, and lowering of leachate at waste disposal sites. Biochar has been utilized as a carrier to support metal ferrite in the development of MFBC nanocomposites. These MFBC nanocomposites offer great potential to enhance wastewater treatment via synergistic adsorption and photocatalytic dye degradation. It does not only accelerate the photocatalytic degradation of dye pollutants but also ensures the restoration of ecological balance without producing hazardous materials and regenerated by magnetic separation. Emerging trends include ternary hybrids (e.g., MFBC/g-C_3N_4) for multiple removal of pollutants, integration of advanced oxidation processes, and utilization of highly produced waste-derived biochar for sustainability. The optimizations of MFBCs could be the transition to cost-effective, eco-friendly solutions for industrial-scale dye remediation that potentially reducing the reliance on traditional adsorbents like AC. However, realizing these prospects requires in-depth mechanistic studies on multi-pollutant interactions with MFBC nanocomposites. Large-scale production of MFBCs encounters significant challenges, primarily associated with synthesis strategies and structural uniformity. Chemical methods such as co-precipitation and sol–gel synthesis is advantageous in controlling particle size but yield poor crystallinity and undesirable byproducts limiting their viability for large-scale production. Physical methods such mechanical mixing and ball milling produces higher yield yet compromises to structural integrity and uniformity in particle size and often led to intensify agglomeration owing to the intrinsic magnetic interactions of ferrites. Hydrothermal and solvothermal techniques are constrained by equipment safety concerns and limited batch capacity, while high-temperature pyrolysis during biochar production can release hazardous volatiles increasing both environmental risk and processing costs. Furthermore, achieving homogeneous dispersion of ferrite nanoparticles on biochar matrices remains a critical obstacle, hindering scalability for dye adsorption, and photocatalytic applications. Addressing these key challenges requires the development of environmental benign and sustainable synthesis routes and cost-effective batch technologies to ensure product uniformity and applicability at an industrial scale.

This review article summarizes the advances and modifications implemented in the synthesis of MFBC nanocomposites in remediation of textile dye effluents. The treatment of textile industrial wastewater requires a great deal of research in developing cost-efficient, recyclable and effective materials that can be employed in removing dye pollutants. The photodegradation efficiency of different MFBC nanocomposites depends on several factors such as magnetic properties, band gap energy, specific surface area, charge separation efficiency whereas the adsorption capacity has been influenced by surface morphology, functional groups interactions, surface-to-volume ratio, temperature, pH and contact time. The performance of various nanocomposites synthesized via different methods such as hydrothermal, co-precipitation, sol-gel and one-step pyrolysis was assessed by their adsorption capacity or photocatalytic activity. The synergistic effect of adsorption and photocatalytic degradation paves a significant pathway in effective removal of dye effluents. The strategic development of MFBC nanocomposite can be focused on enhancing the specific surface area, tunable porosity to leverage the active sites, and harness the visible light-harvesting efficiency for maximum adsorption and photodegradation of dyes. While MFBC nanocomposites offers tremendous potential for wastewater purification due to their multifunctional capabilities, their large-scale implementation is still limited. In the near future, comprehensive research must be directed toward evaluating their technical viability in real-world scenarios. A life cycle assessment (LCA) is essential to evaluate the environmental sustainability of nanocomposite synthesis, regeneration and disposal. This include quantifying the energy input, carbon footprint, and long-term ecological impacts. Attention must be given to toxic intermediate by-products that may form during photocatalysis or adsorption processes, which can sometimes exhibit higher toxicity than the parent pollutants. In addition, the reusability and recyclability of nanocomposites to remove dye pollutants poses significant importance in wastewater treatment process.

Author Contributions

S.B.: Writing—review & editing; supervision; resources; validation; conceptualization. **H.Z.**: Writing—original draft; visualization; investigation; data curation. **A.B.**: Visualization & formal analysis.

Acknowledgments

One of the author Hozefa Dhila would like to acknowledge Symbiosis Centre for Research and Innovation (SCRI) for Research Fellowship.

Conflict of Interests

The authors declare no conflict of interest.

Data Availability Statement

The data that support the findings of this study are available from the corresponding author upon reasonable request.

Keywords: Adsorption · Biochar · Dye · Nanocomposites · Photocatalytic degradation · Spinel ferrites

[1] G. Tripathi, A. Husain, S. Ahmad, Z. Hasan, A. Farooqui, in *Contamination of Water*, Elsevier, **2021**, pp. 85–98, https://doi.org/10.1016/B978-0-12-824058-8.00017-7.
[2] N. Zulfiqar, M. T. Shafi, M. A. Ali, N. Mansha, F. Inam, *IJSEE* **2025**, *2*, 63–69.
[3] D. Patel, A. Singh, S. R. Ambati, R. S. Singh, R. K. Sonwani, *J. Environ. Manage.* **2024**, *370*, 122804.
[4] A. Tkaczyk, K. Mitrowska, A. Posyniak, *Sci. Total Environ.* **2020**, *717*, 137222.
[5] A. M. S. Jorge, K. K. Athira, M. B. Alves, R. L. Gardas, J. F. B. Pereira, *J. Water Proc. Eng.* **2023**, *55*, 104125.
[6] P. S. Kumar, K. G. Pavithra, Water in Textiles and Fashion **2019**, Ch. 2, pp. 21–40, https://doi.org/10.1016/B978-0-08-102633-5.00002-6.
[7] A. Haleem, M. Ullah, S. ur Rehman, A. Shah, M. Farooq, T. Saeed, I. Ullah, H. Li, *Water* **2024**, *16*, 1588.
[8] A. Saravanan, P. Senthil Kumar, S. Jeevanantham, S. Karishma, B. Tajsabreen, P. R. Yaashikaa, B. Reshma, *Chemosphere* **2021**, *280*, 130595.
[9] M. G. Gote, H. H. Dhila, S. R. Muley, *Nat. Environ. Poll. Technol.* **2023**, *22*, 39–61.
[10] R. Al-Tohamy, S. S. Ali, F. Li, K. M. Okasha, Y. A.-G. Mahmoud, T. Elsamahy, H. Jiao, Y. Fu, J. Sun, *Ecotoxicol. Environ. Saf.* **2022**, *231*, 113160.
[11] J. Ayach, W. El Malti, L. Duma, J. Lalevée, M. Al Ajami, H. Hamad, A. Hijazi, *Polymers* **2024**, *16*, 1959.
[12] B. M. Adesanmi, Y.-T. Hung, H. H. Paul, C. R. Huhnke, *GSC Adv. Res. Rev.* **2022**, *10*, 126–137.
[13] C. R. Holkar, A. J. Jadhav, D. V. Pinjari, N. M. Mahamuni, A. B. Pandit, *J. Environ. Manga.* **2016**, *182*, 351–366.
[14] B. A. Kusumlata, A. Kumar, S. Gautam, *Limnol. Rev.* **2024**, *24*, 126–149.
[15] S. Dutta, B. Gupta, S. K. Srivastava, A. K. Gupta, *Mater. Adv.* **2021**, *2*, 4497–4531.
[16] A. Haleem, A. Shafiq, S.-Q. Chen, M. Nazar, *Molecules* **2023**, *28*, 1081.
[17] J. Guo, T. Zhou, H. Guo, C. Ge, J. Lu, *J. Eng. Fib. Fabr.* **2025**, *20*, 1–27.
[18] A. R. Bhapkar, S. Bhame, *J. Environ. Chem. Eng.* **2024**, *12*, 112553.
[19] A. R. Bhapkar, M. Geetha, D. Jaspal, K. Gheisari, M. Laad, J.-J. Cabibihan, K. K. Sadasivuni, S. Bhame, *Appl. Nanosci.* **2023**, *13*, 5777–5793.
[20] A. R. Bhapkar, H. Dhila, R. Prasad, K. Gheisari, K. K. Sadasivuni, S. Bhame, *JWPE* **2025**, *69*, 106750.
[21] N. V. Iyer, G. L. Agawane, A. Bhapkar, J. A. Kher, S. D. Bhame, *J. Water Environm. Nanotechnol.* **2023**, *8*, 23–33.
[22] S. Khan, T. Noor, N. Iqbal, L. Yaqoob, *ACS Omega* **2024**, *9*, 21751–21767.
[23] E. H. Khader, S. A. Muslim, N. M. C. Saady, N. S. Ali, I. K. Salih, T. J. Mohammed, T. M. Albayati, S. Zendehboudi, *Desal. Water Treat.* **2024**, *318*, 100384.
[24] H. Dhila, A. Bhapkar, S. Bhame, *Desalination and Water Treatment* **2025**, *321*, 101004.
[25] A. Bhapkar, R. Prasad, D. Jaspal, M. Shirolkar, K. Gheisari, S. Bhame, *Inorg. Chem. Commun.* **2023**, *148*, 110311.
[26] N. Zulfiqar, R. Nadeem, O. A. Musaimi, *ACS Omega* **2024**, *9*, 29205–29225.
[27] H. Qin, Y. He, P. Xu, D. Huang, Z. Wang, H. Wang, Z. Wang, Y. Zhao, Q. Tian, C. Wang, *Adv. Colloid Interface Sci.* **2021**, *294*, 102486.
[28] S. J. Salih, W. M. Mahmood, *Heliyon* **2023**, *9*, e16601.
[29] Y. Cheng, S. Zhang, Z. Wang, B. Wang, J. You, R. Guo, H. Zhang, *Sep. Purif. Technol.* **2023**, *318*, 123971.
[30] E. Casbeer, V. K. Sharma, X.-Z. Li, *Sep. Purif. Technol.* **2012**, *87*, 1–14.
[31] M. G. Gonçalves, P. A. da Silva Veiga, M. R. Fornari, P. Peralta-Zamora, A. S. Mangrich, S. Silvestri, *Sci. Total Environ.* **2020**, *748*, 141381.
[32] K. K. Kefeni, B. B. Mamba, *Sustainable Mater. Technol.* **2020**, *23*, e00140.
[33] S. Singh, A. K. Atri, I. Qadir, S. Sharma, U. Manhas, D. Singh, *ACS Omega* **2023**, *8*, 6302–6317.
[34] A. Aslam, M. Z. Abid, K. Rafiq, A. Rauf, E. Hussain, *Sci. Rep.* **2023**, *13*, 6306.
[35] S. Nadeem, M. Bukhari, M. Javed, S. Iqbal, M. N. Ahmad, H. Alrbyawi, M. M. Al-Anazy, E. B. Elkaeed, H. H. Hegazy, M. A. Qayyum, R. A. Pashameah, E. Alzahrani, A.-E. Farouk, *Molecules* **2022**, *27*, 7677.
[36] J. Kahkeci, M. Gamal El-Din, *Chem. Eng. J.* **2023**, *476*, 146530.
[37] M. Sajid, M. Asif, N. Baig, M. Kabeer, I. Ihsanullah, A. W. Mohammad, *JWPE* **2022**, *47*, 102815.
[38] F. D. Prochnow, M. Cavali, A. P. Dresch, I. M. Belli, N. Libardi, A. B. de Castilhos, *Processes* **2024**, *12*, 1006.
[39] T. K. Bui, L. T. Nguyen, T. M. Cao, V. Van Pham, **2024**, 1–21.
[40] A. Chakraborty, B. Bhattacharjee, M. Ahmaruzzaman, *Inorg. Chem. Commun.* **2025**, *171*, 113444.
[41] D. Paraschiv, C. Tudor, R. Petrariu, *Sustainability* **2015**, *7*, 1280–1291.
[42] Z. Xiong, Z. Huanhuan, W. Jing, C. Wei, C. Yingquan, X. Gao, Y. Haiping, C. Hanping, *Biochar* **2021**, *3*, 657–670.
[43] A. Waheed, H. Xu, X. Qiao, A. Aili, Y. Yiremaikebayi, D. Haitao, M. Muhammad, *Biomass Bioenergy* **2025**, *193*, 107531.
[44] K. Kameyama, T. Miyamoto, Y. Iwata, T. Shiono, *Soil Science and Plant Nutrition* **2016**, *62*, 180–184.
[45] N. A. S. Mohammed, R. A. Abu-Zurayk, I. Hamadneh, A. H. Al-Dujaili, *J. Environ. Manag.* **2018**, *226*, 377–385.
[46] M. Uchimiya, L. H. Wartelle, K. T. Klasson, C. A. Fortier, I. M. Lima, *J. Agric. Food Chem.* **2011**, *59*, 2501–2510.
[47] J. Wang, S. Wang, *J. Cleaner Prod.* **2019**, *227*, 1002–1022.
[48] J. Chen, J. Zhou, W. Zheng, S. Leng, Z. Ai, W. Zhang, Z. Yang, J. Yang, Z. Xu, J. Cao, M. Zhang, L. Leng, H. Li, *Sci. Total Environ.* **2024**, *946*, 174081.
[49] S. Rana, A. Kumar, P. Dhiman, G. Sharma, T. Wang, *Journal of Rare Earths* **2024**, *43*, 1571–1589.
[50] S. Sri Shalini, K. Palanivelu, A. Ramachandran, V. Raghavan, *Biomass Convers. Biorefin.* **2021**, *11*, 2247–2267.
[51] L. Leng, Q. Xiong, L. Yang, H. Li, Y. Zhou, W. Zhang, S. Jiang, H. Li, H. Huang, *Sci. Total Environ.* **2021**, *763*, 144204.
[52] B. Qiu, Q. Shao, J. Shi, C. Yang, H. Chu, *Sep. Purif. Technol.* **2022**, *300*, 121925.
[53] N. Zulfiqar, M. Ali, F. Inam, S. Khawaja, H. A. Raza, F. Khan, *Dis. Appl. Sci.* **2025**, *7*, 558.
[54] H. Asif, R. Munir, G. Albasher, M. Sayed, A. Muneer, A. Mansha, F. Younas, S. Noreen, *AQUA — Water Infrastructure, Ecosystems and Society* **2024**, *73*, 266–285.
[55] P. A. Ajibade, E. C. Nnadozie, *ACS Omega* **2020**, *5*, 32386–32394.
[56] I. Fatimah, G. Purwiandono, I. Sahroni, A. Wijayana, M. Faraswati, A. Dwi Putri, W.-C. Oh, R. Doong, *Environ. Nanotechnol. Mon. Manage.* **2022**, *17*, 100669.
[57] S. E. Shirsath, D. Wang, S. S. Jadhav, M. L. Mane, S. Li, in *Handbook of Sol-Gel Science and Technology*, Springer International Publishing, Cham **2018**, 1–41.
[58] J. Leichtweis, N. Welter, Y. Vieira, S. Silvestri, E. Carissimi, *EMA* **2022**, *194*, 907.
[59] J. Leichtweis, S. Silvestri, N. Welter, Y. Vieira, P. I. Zaragoza-Sánchez, A. C. Chávez-Mejía, E. Carissimi, *Process Saf. Environ. Prot.* **2021**, *150*, 497–509.
[60] N. Welter, J. Leichtweis, S. Silvestri, P. I. Z. Sánchez, A. C. C. Mejía, E. Carissimi, *J. Alloys Compd.* **2022**, *901*, 163758.
[61] H. Fan, C. Chen, Q. Huang, J. Lu, J. Hu, P. Wang, J. Liang, H. Hu, T. Gan, *Environ. Sci. Pollut. Res.* **2022**, *30*, 38775–38793.
[62] X. Meng, Y. Li, Y. Liu, R. Zhou, Y. Fu, J. Chen, *RSC Adv.* **2023**, *13*, 24819–24829.
[63] A. M. Abdelfatah, M. Fawzy, M. E. El-Khouly, A. S. Eltaweil, *Biomass Convers. Biorefin.* **2024**, https://doi.org/10.1007/s13399-024-05327-5.
[64] Z. Wu, X. Wang, J. Yao, S. Zhan, H. Li, J. Zhang, Z. Qiu, *Sep. Purific. Technol.* **2021**, *277*, 119474.
[65] Z. Cheng, S. Li, T. T. Nguyen, X. Gao, S. Luo, M. Guo, *Colloids Surf. A* **2021**, *631*, 127651.
[66] Z. Cheng, S. Luo, X. Li, S. Zhang, T. Thang Nguyen, M. Guo, X. Gao, *Appl. Surf. Sci.* **2021**, *566*, 150654.

[67] R. Kaveh, M. Mortazavi, H. Alijani, M. Abdouss, A. S. Dehkalani, S. Mazinani, *J. Solid State Chem.* **2024**, *331*, 124503.

[68] Z. Guo, R. Chen, R. Yang, F. Yang, J. Chen, Y. Li, R. Zhou, J. Xu, *Sci. Total Environ.* **2020**, *722*, 137822.

[69] A. F. Alharbi, A. A. Alotaibi, H. E. M. Gomaa, A. A. M. Abahussain, S. M. Abdel Azeem, *Adsorpt. Sci. Technol.* **2023**, *2023*, 9993465.

[70] N. Shabelskaya, M. Egorova, A. Radjabov, M. Burachevskaya, I. Lobzenko, T. Minkina, S. Sushkova, *Water* **2022**, *15*, 93.

[71] C. Chen, W. Gao, H. Fan, X. Huang, Z. Tong, *J. Taiwan Inst. Chem. Eng.* **2024**, *163*, 105641.

[72] R. Meena, M. M. S. Abdullah, V. Vasanthakumar, D. Ravichandran, S. Murugesan, *Ionics* **2024**, *30*, 5639–5650.

[73] D. T. C. Nguyen, A. A. Jalil, N. C. Huynh, L. Q. Phan, D. V. N. Vo, T. Van Tran, *J. Chem. Technol. Biotechnol.* **2023**, *98*, 2655–2667.

[74] R. Foroutan, R. Mohammadi, B. Ramavandi, *Environ. Sci. Pollut. Res.* **2019**, *26*, 19523–19539.

[75] G. Ma, D. Lan, Y. Zhang, X. Sun, Z. Jia, G. Wu, G. Bu, P. Yin, *Small* **2024**, *20*, 2404449.

[76] N. Zulfiqar, F. Inam, *SSRN Electro. J.* **2025**, *15*, 721.

[77] J. Du, W. Xu, J. Liu, Z. Zhao, *J. Chem. Technol. Biotechnol.* **2020**, *95*, 1135–1145.

[78] R. D, M. A. Megala, K. Anbalagan, P. Srivastava, M. A. Al-Dosary, A. A. Hatamleh, *Colloids Surf. A* **2025**, *713*, 136465.

[79] J. Leichtweis, N. Welter, Y. Vieira, T. R. Storck, B. Clasen, S. Silvestri, E. Carissimi, *J. photochem. photobiol., A Chem* **2023**, *440*, 114676.

[80] J. Leichtweis, Y. Vieira, S. Silvestri, G. L. Dotto, E. Carissimi, *Colloids Surf. A* **2023**, *677*, 132364.

[81] Y. Zheng, J. Fan, J. Cui, B. Yang, *ChemistrySelect* **2024**, *9*, e202302952.

[82] A. Qureashi, F. A. Ganaie, A. Bashir, I. Nazir, Z. ul Haq, L. A. Malik, K. Fatima, A. Y. A. Alzahrani, A. H. Pandith, *New J. Chem.* **2024**, *48*, 8479–8494.

[83] J. Leichtweis, A. C. Ferreira Piazzi Fuhr, N. Welter, L. G. Ramírez Mérida, E. Carissimi, *WBV* **2025**, 031145.

[84] N. P. Shabelskaya, A. V. Arzumanova, Y. A. Gaidukova, S. I. Sulima, E. V. Vasileva, E. A. Yakovenko, *Adv. Nat. Sci. Nanosci. Nanotechnol.* **2023**, *14*, 045002.

[85] A. Ahmadi, R. Foroutan, H. Esmaeili, S. J. Peighambardoust, S. Hemmati, B. Ramavandi, *Mater. Chem. Phys.* **2022**, *284*, 126088.

[86] M. Zarei, T. Ebadi, B. Ramavandi, S. J. Peighambardoust, *Surfaces and Interfaces* **2023**, *43*, 103571.

[87] S. J. Olusegun, E. T. F. Freitas, L. R. S. Lara, N. D. S. Mohallem, *Environ. Technol. (U.K.)* **2021**, *42*, 2163–2176.

[88] J. Sun, X. Lin, J. Xie, Y. Zhang, Q. Wang, Z. Ying, *Colloids Surf. A* **2020**, *606*, 125556.

[89] A. Sharma, S. Rasheed, D. Mangla, A. Choudhry, S. Shukla, S. A. Chaudhry, *ChemistrySelect* **2023**, *8*, e03709.

[90] Y. Cheng, A. Li, W. Shi, L. Zhao, *Chem. Eng. J.* **2024**, *481*, 148535.

[91] F. Bazipour, S. Jorfi, H. Maleki, A. Babaei, *Water, Air, Soil Pollut.* **2024**, *235*, 811.

[92] N. C. S. de Souza, G. do Carmo Dias, G. A. Puiatti, K. L. A. de Oliveira, T. B. Vitorino, T. A. Silva, R. P. L. Moreira, *Int. J. Environ. Sci. Technol.* **2025**, *22*, 4263–4280.

[93] J. Leichtweis, N. Welter, Y. Vieira, T. R. Storck, B. Clasen, S. Silvestri, E. Carissimi, *Environ. Technol.* **2025**, *46*, 1268–1279.

[94] Q. Huang, C. Chen, X. Zhao, X. Bu, X. Liao, H. Fan, W. Gao, H. Hu, Y. Zhang, Z. Huang, *J. Environ. Chem. Eng.* **2021**, *9*, 105800.

[95] A. Sharma, A. Choudhry, B. Mangla, S. A. Chaudhry, *Clean Technol. Environ. Policy* **2023**, *26*, 3921–3935.

[96] M. A. Amjed, X. Wu, I. Ali, I. Naz, M. Dai, A. Tehrim, W. Niaz, S. F. Javaid, C. Peng, *J. Chem. Technol. Biotechnol.* **2021**, *96*, 2310–2324.

[97] M. E. Mahmoud, S. M. El-Bahy, S. M. T. Elweshahy, *Bioresour. Technol.* **2021**, *342*, 126029.

[98] A. Choudhry, A. Sharma, S. I. Siddiqui, I. Ahamad, M. Sajid, T. A. Khan, S. A. Chaudhry, *Environ. Res.* **2023**, *220*, 115193.

[99] A. S. El-Kalliny, M. S. Abdel-Wahed, N. A. Abdel-Hady, A. M. Abd El-Aty, M. I. Badawy, T. A. Gad-Allah, *Sep. Purif. Technol.* **2024**, *330*, 125497.

[100] H. Fu, S. Ma, P. Zhao, S. Xu, S. Zhan, *Chem. Eng. J.* **2019**, *360*, 157–170.

[101] X. Jiang, Z. Tan, G. Jiang, C. Liu, G. Gao, Z. Liu, *ACS Omega* **2024**, *9*, 6455–6465.

[102] M. Maqbool, R. Munir, F. Younas, A. Muneer, M. F. Sardar, R. Nadeem, M. Zahid, M. Yaseen, G. Albasher, S. Noreen, *J. Inorg. Organomet. Polym. Mater.* **2024**, *34*, 3786–3816.

[103] G. Rathi, V. Singh, S. A. Chaudhry, *ChemistrySelect* **2023**, *8*, e02199.

[104] Z. Wang, Y. Li, X. Xie, Z. Wang, *Colloids Surf. A* **2021**, *613*, 126104.

[105] H. Zeghioud, S. Mouhamadou, *Water, Air, Soil Pollut.* **2023**, *234*, 233.

[106] P. Sirajudheen, P. Karthikeyan, K. Ramkumar, P. Nisheetha, S. Meenakshi, *J. Mol. Liq.* **2021**, *327*, 114829.

[107] S. I. Siddiqui, S. A. Chaudhry, *J. Cleaner Prod.* **2018**, *200*, 996–1008.

[108] T. S. Saleh, A. K. Badawi, R. S. Salama, M. M. M. Mostafa, *Materials* **2023**, *16*, 2170.

[109] G. Mustafa, R. Munir, B. Sadia, F. Younas, M. Sayed, A. Muneer, M. F. Sardar, G. Albasher, S. Noreen, *J. Environ. Chem. Eng.* **2024**, *12*, 112581.

[110] M. J. Livani, M. Ghorbani, *Environ. Technol.* **2018**, *39*, 2977–2993.

[111] D. T. C. Nguyen, A. A. Jalil, N. S. Hassan, M. B. Bahari, *Mater. Chem. Phys.* **2025**, *334*, 130460.

[112] X. Cai, J. Li, Y. Liu, X. Hu, X. Tan, S. Liu, H. Wang, Y. Gu, L. Luo, *IJERPH* **2020**, *17*, 6.

[113] S. Perveen, R. Nadeem, S. Ali, Y. Jamil, *Zeitschrift fur Physikalische Chemie* **2021**, *235*, 1721–1745.

[114] S. Perveen, R. Nadeem, F. Nosheen, M. I. Asjad, J. Awrejcewicz, T. Anwar, *Nanomaterials* **2022**, *12*, 2828.

[115] J. Zhang, M. Liu, T. Yang, K. Yang, H. Wang, *Water Sci. Technol.* **2016**, *74*, 1971–1979.

[116] Y. Meng, D. Chen, Y. Li, W. Sheng, Y. Lin, H. Yang, G. Qian, *Environ. Eng. Res.* **2024**, *29*, 240028–0.

[117] G. Yadav, S. R. Mishra, V. Gadore, N. Yadav, M. Ahmaruzzaman, *Sci. Rep.* **2023**, *13*, 12940.

[118] N. T. T. Nguyen, T. T. Tran, T. Van Lam, S. C. Phung, D. T. C. Nguyen, *Arab. J. Sci. Eng.* **2024**, *49*, 8147–8161.

[119] Q. Wen, Y. Chen, X. Rao, R. Yang, Y. Zhao, J. Li, S. Xu, Z. Liang, *Bioresour. Technol.* **2022**, *350*, 126860.

Manuscript received: July 9, 2025